

Observational estimate of the partial covering probability of quasar emission regions by distant H₂ absorption clouds

V. V. Klimenko,^{1★} P. Petitjean² and A. V. Ivanchik¹

¹*Ioffe Institute, Polytechnicheskaya ul. 26, Saint Petersburg, 194021, Russia*

²*Institut d'Astrophysique de Paris, Sorbonne Universités & CNRS, UMR 7095, 98bis bd Arago, F-75014 Paris, France*

Accepted 2020 February 28. Received 2020 February 27; in original form 2019 August 20

ABSTRACT

We have searched high spectral resolution spectra of quasars known to exhibit high redshift ($z > 1.7$) intervening H₂-bearing damped Lyman- α (DLA) systems for partial coverage of the quasar emission by intervening H₂ clouds. Partial coverage manifests itself by the presence of non-zero residual flux in the core of saturated H₂ absorption lines. The residual flux can be observed either only at the bottom of absorption lines redshifted on top of quasar emission lines, in which case part of the broad line region (BLR) is not covered, or in all absorption lines, in case some continuum source is not covered. Among 35 H₂ absorption clouds in 14 quasar spectra obtained with the VLT-UVES or Keck-HIRES spectrographs, we detect partial coverage of the BLR for 13 clouds. This result suggests that the probability of partial coverage of the QSO BLR by a distant H₂ absorption cloud is about 40 per cent. For four systems towards Q 0013–0029, Q 0405–4418, Q 0812+3208, and J 2100–0641, partial coverage is detected for the first time. We determine the theoretical probability of partial coverage of the BLR by a distant H₂ cloud as a function of the ratio between the cloud and the BLR sizes. Using this model, we obtain an estimate of the characteristic BLR radius of 50^{+19}_{-23} light days. This is similar to the estimate of the BLR size obtained by reverberation-mapping analysis (~ 100 light days).

Key words: ISM: clouds – ISM: molecules – quasars: absorption lines – cosmology: observations.

1 INTRODUCTION

Partial coverage of a background quasar emission manifests itself as the presence of a non-zero flux in the core of otherwise saturated absorption lines. This is most of the time due to gas clouds located in the quasar vicinity, i.e. $z_{\text{abs}} \sim z_{\text{em}}$ (so-called intrinsic absorptions, e.g. Petitjean, Rauch & Carswell 1994; Barlow, Hamann & Sargent 1997). The detection of partial coverage together with time variability of the residual flux is sometimes used to distinguish intrinsic from intervening ('distant') absorbers (Barlow et al. 1997).

The first case of partial coverage by a high redshift intervening C I and H₂ absorber was observed in the quasar spectrum of Q1232+0815 (Ivanchik et al. 2010). Balashev et al. (2011) have studied this partial coverage and explained that the quasar broad line region (BLR) at $z_{\text{em}} = 2.57$ was not completely covered by an H₂ molecular cloud in a distant galaxy at $z_{\text{abs}} = 2.33$. A sign of partial coverage was also observed in Mg II absorption lines of intervening systems in front of QSO APM08279+5255 (Ellison

et al. 1999; Petitjean et al. 2000; Ellison et al. 2004) but has been demonstrated to be caused by multiple lensing of the quasar.

Unlike most of the intervening absorbers detected by metal absorptions (Mg II, C IV, and others) or HI absorptions, which have typical dimensions of ~ 1 kpc or more, molecular clouds (H₂) are compact, of size about 1 pc, and can cover incompletely the emission region of the background quasar. This gives us the unique opportunity to study the structure of the quasar emission region. Moreover, the effect of partial coverage can play an important role in the analysis of the absorption system itself (e.g. Balashev et al. 2011; Klimenko et al. 2015).

Until recently, partial coverage has been considered as a rare effect for intervening absorption systems. Ofengeim et al. (2015) have theoretically estimated a lower limit for the detection probability of partial coverage of the QSO BLR by distant molecular hydrogen clouds and found it to be higher than 10 per cent. At present, among about 40 known H₂ absorption systems at high redshift, eight cases of partial covering of the BLR have been reported: for three absorption systems, partial coverage was found in H₂ lines redshifted on top of the quasar Ly β emission line [Q 1232+082 Balashev et al. (2011), Q 0643–5041 Alborno Vázquez et al. (2014), and J 2123–0050 Klimenko et al. (2016)]; for three systems,

* E-mail: slava.klimenko@gmail.com

it was found in C I lines redshifted on top of the C IV emission line [J 1439+1118, and Q 2340–0053 Bergeron & Boissé (2017), J 2225+0527 Krogager et al. (2016)], and one system in S II lines redshifted on top of the Ly α emission line [J 0843+0221 Balashev et al. (2017)]. Additionally, in one system partial coverage of some continuum emission source has been observed in H₂ lines over the whole wavelength range of the QSO 0528–2508 Lyman- α forest (Klimenko et al. 2015). Residual flux observed in the H₂ system towards Q 0643–5041 (Albornoz Vásquez et al. 2014) can also be caused by partial covering of the quasar continuum source.

In this paper, we analyse H₂ and C I absorption lines in a sample of 18 quasar spectra bearing intervening H₂ absorption systems. We present an independent observational estimate of the probability for partial coverage of the quasar emission by high redshift H₂ absorption clouds.

2 SAMPLE

The amount of residual flux left at the bottom of H₂ absorption lines in case of partial coverage of a QSO BLR or continuum sources does not exceed 2–7 per cent of the total quasar flux (e.g. analysis of H₂ lines in Q 0528–2508 Klimenko et al. 2015, Q 1232+082 Balashev et al. 2011, and others), and it can easily be missed in small or intermediate resolution spectra. Therefore, in order to obtain a reliable estimate of the partial coverage probability, we analysed quasar spectra with high spectral resolution ($R \sim 45000$) and high signal-to-noise ratio $S/N > 10$ available to us. Such spectra were observed either with the Ultraviolet and Visual Echelle Spectrograph (UVES, Dekker et al. 2000) mounted on the ESO VLT-UT 2 8.2 m telescope on Cerro Paranal, Chile, or with the High Resolution Echelle Spectrometer (HIRES, Vogt et al. 1994) on the Keck I telescope on Maunakea in Hawaii. For the same reason, we did not include spectra obtained with medium spectral resolution (e.g. observed with VLT/X-shooter).

The list of H₂-bearing quasar spectra considered in the analysis is presented in Table 1. For each H₂ absorption system, we give the name of the quasar (column #1), its emission redshift (column #2), the redshifts of its velocity components (column #3), the total H I column density (column #4), their H₂ column density (column #5), the name of the emission line on top of which partial coverage is seen (column #6), the species (H₂ or C I) that was used for the residual flux estimate (column #7), the value of the residual flux (column #8), the value of the covering factor (column #9) and the estimates of the hydrogen density (column #10), and the physical size of the absorber (column #11). This sample of quasars is called the S⁰ sample.

The blue end of the UVES and KECK spectrographs (3100 Å) limits the redshift of intervening H₂ absorption systems to $z_{\text{abs}} \geq 1.9$ so that at least several absorption lines of H₂ are redshifted inside the observable wavelength range. We thus select spectra with the condition $(1 + z_{\text{qso}}) 1025 \text{ \AA} \leq (1 + z_{\text{abs}}) 1110 \text{ \AA}$, so that at least one H₂ Lyman band [$\lambda(\text{LOP1}) = 1110 \text{ \AA}$] covers the Ly β emission blend [$\lambda(\text{OVI} - \text{Ly}\beta) = 1025 - 1035 \text{ \AA}$]. The application of this condition defines a new sample of spectra (S¹). For systems in sample S¹, we can detect partial coverage of the QSO BLR with a high probability. The S¹ sample is complete when searching for partial coverage of the quasar BLR. Since most of these systems were discovered in high-resolution quasar spectra after a blind search for H₂ in absorption systems, we can assume that there is no observational bias in this sample. For the spectra that are not included in the S¹ sample,

we also check for the presence of partial coverage of the quasar continuum emission source.

The observations and data reduction procedures are described in detail in Petitjean, Srianand & Ledoux (2002) for Q 0013-0029, Noterdaeme et al. (2007b) for HE 0027–1836, Ledoux, Petitjean & Srianand (2003) for Q 0347–383, Ledoux et al. (2003) for Q 0405–4418, Klimenko et al. (2015) for Q 0528–2508, Ledoux, Srianand & Petitjean (2002) for Q 0551–3637, Albornoz Vásquez et al. (2014) for Q 0643–5041, Balashev, Ivanchik & Varshalovich (2010) for Q 0812+3208 (Keck), Guimarães et al. (2012) for Q 0816+1446, Balashev et al. (2017) for Q 0843+0221, Balashev et al. (2011) for Q 1232+0815, Noterdaeme et al. (2010) for J 1237+0647, Srianand et al. (2008) for J 1439+1117, Ledoux, Petitjean & Srianand (2006) for J 1443+2724, Ledoux et al. (2003) for Q 1444+0126, Noterdaeme et al. (2015) for J 1456+1609, Balashev et al. (2015) for J 2100–0641, Klimenko et al. (2016) for J 2123–0050, Jorgenson, Wolfe & Prochaska (2010) for Q 2340–0053, and Noterdaeme et al. (2007a), Jorgenson et al. (2010) for Q 2348–0108.

We consider the various velocity components of the H₂ absorbing systems as independent absorbing clouds. In total, we have 35 H₂ clouds in 14 quasar spectra in the S¹ sample and 41 H₂ clouds in 18 quasar spectra in the S⁰ sample.

3 ANALYSIS

We analyse the H₂ and C I absorption systems detected in the quasar spectra of the S⁰ sample and search for residual flux in the core of saturated absorption lines. We determine their parameters using the following procedures.

3.1 Absorption lines analysis

To analyse absorption lines, we use a code that simultaneously fits absorption profiles of selected species using Voigt profiles convolved with the instrumental response function. We use the χ^2 likelihood function, which assumes that uncertainties in the spectrum have a Gaussian probability distribution function. The shape of the likelihood function is defined by the Monte Carlo Markov Chain approach with implementation of the affine-invariant ensemble sampler (Goodman & Weare 2010). Such a technique ensures that we confidently find the global maximum in the parametric space and provides a reliable estimate of statistical errors on the parameters.

Partial coverage is taken into account by including an additional residual flux in the core of absorption lines located on top of quasar emission lines (case 1) or a uniform additional residual flux in the core of absorption lines over the whole spectrum (case 2). For each spectral pixel, we can write

$$F_{\text{obs}}(\lambda) = F_{\text{add}} + (F_{\text{tot}} - F_{\text{add}}) \exp(-\tau(\lambda)) \\ = \text{LFR} \times F_{\text{tot}} + (1 - \text{LFR}) F_{\text{tot}} \exp(-\tau(\lambda)) \quad (1)$$

where F_{tot} is the total flux of the background source constructed by fitting spline to selected continuum regions devoid of any absorption. F_{add} is the flux produced by the uncovered sources, τ is the optical depth of the absorption at wavelength λ . The line flux residual (LFR) is the fraction of the quasar total flux that passes by the cloud and is an additional fitting parameter.

$$\text{LFR} = \frac{F_{\text{add}}}{F_{\text{tot}}} \quad (2)$$

Table 1. List of H₂ absorption systems in the S⁰ sample. The first part of the list belongs to the sample S¹: for which the redshift satisfies the condition: $(1 + z_{\text{abs}})1110 \text{ \AA} > (1 + z_{\text{qso}})1025 \text{ \AA}$. The columns show the data of absorption systems: the redshifts of quasar (2) and absorbing cloud (3), column densities of H I in the DLA system (4) and H₂ (5), the names of the emission line (6) and species (7), which were used for the residual flux estimate, the value of the residual flux (8), the value of the covering factor (9), and our estimates of the hydrogen density (10) and physical size of absorbers (11).

Name	z_{em}	z_{abs}	$\log N_{\text{HI}}^{\text{DLA}}$	$\log N_{\text{H}_2}$	PC	sp	LFR, per cent	f_{cov} , per cent	$\log n$, cm ⁻³	$\log l_c$, cm
Q 0013–0029	2.09	1.966780	20.83 ± 0.05	15.86 ± 0.10	Ly β	H ₂	30 ± 10	10 ⁺³⁰ ₋₁₀		18.24 ^{+0.70} _{-0.63}
		1.966898		15.86 ± 0.15	Ly β	H ₂	24 ± 4	28 ± 12		18.28 ^{+0.67} _{-0.65}
		1.968176		15.40 ± 0.40	Ly β	H ₂	30 ± 10	10 ⁺³⁰ ₋₁₀		18.20 ^{+0.65} _{-0.64}
		1.968250		16.46 ± 0.45	Ly β	H ₂	25 ± 5	25 ± 15		18.32 ^{+0.66} _{-0.72}
		1.9729		18.30 ± 0.30	Ly β	H ₂	<5	>85		18.47 ^{+0.57} _{-0.87}
		1.97380		18.10 ± 0.30	Ly β	H ₂	<7	>79		18.19 ^{+0.84} _{-0.62}
HE 0027–1836	2.55	2.40183	21.75 ± 0.10	17.30 ± 0.07	Ly β	H ₂	<5	>84	<2.21	18.27 ^{+0.75} _{-0.78}
Q 0347–383	3.21	3.024898	20.73 ± 0.05	14.53 ± 0.06	Ly β	H ₂	<10	>68		17.78 ^{+0.61} _{-0.61}
Q 0528–2508	2.78	2.810995	21.35 ± 0.07	18.10 ± 0.01	Ly β	H ₂	<4	>86	2.61 ^{+0.29} _{-0.20}	16.93 ^{+0.53} _{-0.56}
		2.811124		17.82 ± 0.02	Ly β	H ₂	<4	>86	2.56 ^{+0.06} _{-0.04}	16.93 ^{+0.28} _{-0.28}
Q 0812+3208	2.70	2.626443	21.35 ± 0.10	19.93 ± 0.04	Ly β	H ₂	4 ± 1	88 ± 3	2.60 ^{+0.14} _{-0.14}	17.85 ^{+0.26} _{-0.20}
		2.626276		18.82 ± 0.37	Ly β	H ₂	4 ± 1	88 ± 3	1.71 ^{+0.17} _{-0.21}	18.88 ^{+0.38} _{-0.43}
		2.625808		15.98 ± 0.02	Ly β	H ₂	<30	>5	1.69 ^{+0.26} _{-0.23}	18.35 ^{+0.53} _{-0.56}
J 0843+0221	2.92	2.7865	21.82 ± 0.11	21.21 ± 0.02	Ly β	H ₂	<5	>84	2.58 ^{+0.03} _{-0.06}	19.01 ^{+0.18} _{-0.26}
Q 1232+0815	2.57	2.3377	20.90 ± 0.07	19.57 ± 0.10	Ly β	H ₂	6 ± 3	82 ± 10	1.93 ^{+0.10} _{-0.10}	18.76 ^{+0.18} _{-0.28}
J 1237+0647	2.78	2.68801	20.00 ± 0.15	16.28 ± 0.13	Ly β	H ₂	<8	>74	1.00 ^{+0.30} _{-0.90}	18.45 ^{+0.19} _{-0.27}
		2.68868		17.62 ± 0.10	Ly β	H ₂	<8	>74	1.87 ^{+0.11} _{-0.11}	17.99 ^{+0.13} _{-0.25}
		2.68955		19.20 ± 0.13	Ly β	H ₂	<3	>90	1.65 ^{+0.09} _{-0.10}	18.45 ^{+0.11} _{-0.09}
J 1439+1118	2.58	2.418368	20.10 ± 0.10	19.15 ± 0.12	Ly α	C I	7 ± 2	70 ± 15	1.74 ^{+0.12} _{-0.12}	18.45 ^{+0.11} _{-0.10}
		2.418516		18.34 ± 0.35	Ly α	C I	7 ± 2	90 ± 3	1.84 ^{+0.09} _{-0.09}	18.14 ^{+0.14} _{-0.16}
		2.418650		19.09 ± 0.05	Ly α	C I	<10	>85	1.71 ^{+0.12} _{-0.12}	18.45 ^{+0.13} _{-0.10}
J 1443+2724	4.42	4.22371	20.95 ± 0.08	17.91 ± 0.02	Ly β	H ₂	<3	>90		18.28 ^{+0.73} _{-0.76}
		4.22401		18.05 ± 0.05	Ly β	H ₂	<3	>90		18.26 ^{+0.82} _{-0.72}
Q 1444+0126	2.21	2.08680	20.07 ± 0.07	16.49 ± 0.23	Ly β	H ₂	<8	>74		18.13 ^{+0.43} _{-0.62}
		2.08696		18.15 ± 0.10	Ly β	H ₂	<8	>74		17.55 ^{+0.44} _{-0.48}
J 2100–0641	3.14	3.09145	21.05 ± 0.15	18.76 ± 0.03	Ly β	H ₂	9 ± 2	73 ± 10	1.49 ^{+0.38} _{-0.81}	19.00 ^{+0.59} _{-0.64}
J 2123–0050	2.26	2.05930	19.18 ± 0.15	17.94 ± 0.01	Ly β	H ₂	3 ± 1	90 ± 4	1.53 ^{+0.04} _{-0.05}	17.69 ^{+0.06} _{-0.04}
		2.05955		15.16 ± 0.02	Ly β	H ₂	<4	>86	2.06 ^{+0.14} _{-0.12}	17.17 ^{+0.17} _{-0.17}
Q 2340–0053	2.09	2.054164	20.35 ± 0.15	17.43 ± 0.02	Ly β	H ₂	<10	>68	1.86 ^{+0.16} _{-0.18}	18.23 ^{+0.24} _{-0.46}
		2.054288		16.15 ± 0.20	Ly β	H ₂	<30	>5	2.17 ^{+0.26} _{-0.30}	17.42 ^{+0.66} _{-0.54}
		2.054531		18.18 ± 0.02	C IV	C I	17 ± 3	63 ± 7	1.55 ^{+0.07} _{-0.06}	18.66 ^{+0.13} _{-0.11}
		2.054597		17.02 ± 0.42	C IV	C I	15 ⁺² ₋₇	67 ⁺¹⁵ ₋₇	1.70^{+0.70} _{-0.50}	18.33 ^{+0.49} _{-1.27}
		2.054710		17.61 ± 0.04	C IV	C I	<7	>84	1.77 ^{+0.05} _{-0.05}	18.40 ^{+0.11} _{-0.31}
		2.054996		17.94 ± 0.03	Ly β	H ₂	<5	>84	1.93 ^{+0.18} _{-0.20}	18.19 ^{+0.22} _{-0.46}
		2.055135		17.09 ± 0.05	Ly β	H ₂	<5	>84	1.73 ^{+0.18} _{-0.18}	18.34 ^{+0.27} _{-0.40}
(1 + z _{abs})1110 Å < (1 + z _{qso})1025 Å										
Q 0405–4418	3.00	2.59475	21.05 ± 0.10	18.14 ± 0.07	Cont	H ₂	7 ± 1	93 ± 1		17.63 ^{+0.80} _{-0.79}
Q 0551–3637	2.32	1.96214	20.70 ± 0.08	17.42 ^{+0.45} _{-0.73}	Cont	H ₂	<9	>91	2.18 ^{+0.30} _{-0.30}	16.75 ^{+0.62} _{-0.65}
Q 0643–5041	3.09	2.6586	21.03 ± 0.08	18.54 ± 0.01	Cont	H ₂	6 ± 1	94 ± 1		17.71 ^{+0.81} _{-0.75}
Q 0816+1446	3.84	3.28742	22.00 ± 0.10	18.62 ± 0.20	Cont	H ₂	<4	>96	1.88 ^{+0.05} _{-0.05}	17.75 ^{+0.47} _{-0.12}
		3.28667	22.00 ± 0.10	17.60 ± 0.30	Cont	H ₂	<8	>92		18.17 ^{+0.89} _{-0.40}

Cases (1) and (2) correspond to partial coverage of different emission regions of the quasar: the BLR and continuum emission sources, respectively.

We detect partial coverage in 15 out of 41 molecular clouds in the S⁰ sample or 10 out of 18 quasar spectra. We find four new quasars with partial covering in addition to

the six ones already known. The new systems are towards Q 0013–0029, Q 0812+3208, J 2100–0641 (in the S¹ sample), and Q 0405–4418. Specific comments for each of these systems are presented in the next section. A fit to the H₂ absorption lines and corresponding figures are presented in the Appendix A.

3.2 Comments on individual systems

3.2.1 Q 0013–0029

The H₂ absorption system at $z = 1.96$ has six components (Petitjean et al. 2002). For four of them (at $z_{\text{abs}} = 1.966780, 1.966898, 1.968176,$ and 1.968250), we detect the presence of residual flux in the core of saturated H₂ absorption lines of the L2-0 band located on top of the quasar Ly β emission line. From Fig. A1, it is clear that about 20–30 per cent of the quasar emission is not covered. The fit to the H₂ $J = 0$ and $J = 1$ lines for the first four Lyman bands is shown in Fig. A2. Note that the continuum is fully covered.

3.2.2 Q 0405–4418

We detect partial coverage by an H₂ cloud at $z_{\text{abs}} = 2.59473$ in the spectrum of Q 0405–4418. The corresponding LFR is about 7 per cent. In Fig. A3, we show the values of the residual flux in the bottom of saturated $J = 0$ and 1 H₂ absorption lines free from blends versus the observed wavelength (top panel) and versus the product of the oscillator strength by the rest wavelength of H₂ transitions (bottom panel). The fit to the H₂ $J = 0$ and $J = 1$ lines is shown in Fig. A4. We classify this case as partial coverage of continuum sources associated with the quasar.

3.2.3 J 0812+3208

We detect partial coverage the H₂ cloud at $z_{\text{abs}} = 2.626$ in the spectrum of J 0812+3208. The corresponding LFR is about 4 per cent and 2 per cent for the Ly β emission line on the one hand and the C III and Ly ϵ emission lines on the other hand. In Fig. A5, we compare the residual flux in the core of saturated H₂ and Ly α forest lines (blue and orange circles). Lines in the Ly α forest are associated with intergalactic clouds with dimensions larger than several kpc, and thus it is most likely that they cover the background source completely. The flux in cores of the Ly α forest lines is ~ 0.8 per cent with 2 per cent dispersion around this value and is probably due to errors in the background subtraction. By comparison, the LFR measured in the core of H₂ lines of the L4-0 band located on top of the Ly β emission line is 4 ± 1.3 per cent, revealing partial coverage of the BLR. The fit to the H₂ $J = 0$ and $J = 1$ lines is shown in Figs A6–A8.

3.2.4 J 2100–0641

A part of the J2100–0641 spectrum around the position of the Ly β emission line is shown in Fig. A9. We detect some non-zero residual flux in the core of the L5-0 band H₂ lines at $z_{\text{abs}} = 3.092$ located on the top of the emission line Ly β . The corresponding LFR is 9 ± 2 per cent of the total flux. In Fig. A10, we show the values of the residual flux in H₂ $J = 2$ and $J = 3$ lines and in the Ly α forest lines as a function of the observed wavelength. The fit to the H₂ $J = 2$ and $J = 3$ lines by a one-component model is shown in Fig. A11.

3.3 Covering factor measurements

Following previous studies of partial coverage from intervening absorptions (Balashev et al. 2011; Klimenko et al. 2015; Bergeron & Boissé 2017) and associated quasar absorptions (Srianand & Shankaranarayanan 1999; Petitjean et al. 2000; Muzahid et al. 2013), we assume here that the residual flux is the result of some

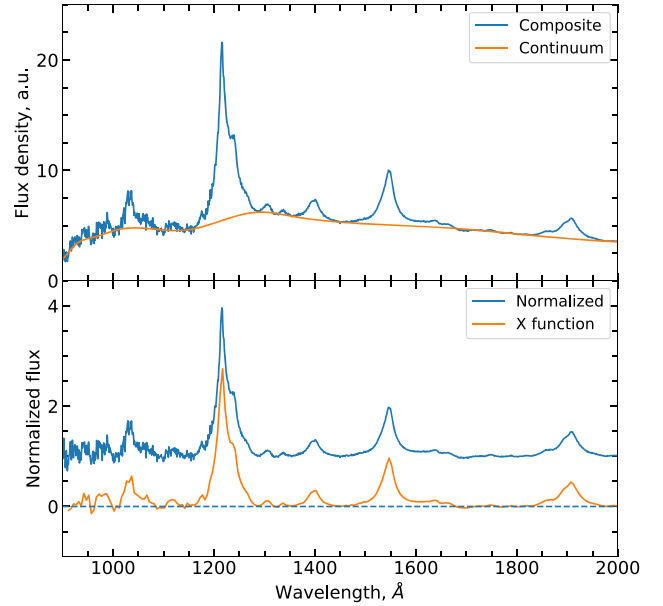


Figure 1. Illustration of the construction of the X function. Top: the blue and orange lines represent the quasar composite spectrum derived by Vanden Berk et al. (2001) and the reconstructed continuum. Bottom: the composite spectrum normalized to the continuum (blue line) and X function ($F_{\text{BLR}}/F_{\text{cont}}$). See text.

radiation emitted by the quasar itself or its surrounding not being covered by the intervening cloud. The covering factor, f , is defined as

$$f = 1 - \frac{F_{\text{add}}}{F_{\text{tot}}} = 1 - \text{LFR} \quad (3)$$

F_{tot} being the total flux and F_{add} the residual flux. In the most general case,

$$F_{\text{add}} = C_{\text{blr}} F_{\text{BLR}} + C_{\text{cont}} F_{\text{cont}} \quad (4)$$

where C_{blr} , C_{cont} are the contributions of, respectively, the BLR and the continuum emissions to the residual flux (see equation 4 in Bergeron & Boissé 2017).

The quasar accretion disc, of size $\sim 10^{15}$ cm (Dai et al. 2010), is much more compact than both the BLRs, of size $\sim 10^{17}$ cm (Kaspi et al. 2017), and the H₂ clouds, of size $\sim 10^{18}$ cm (Balashev et al. 2011; Krogager et al. 2016). Therefore, we suppose that the accretion disc is always covered completely.¹ In most of the spectra in sample S^0 , we do not detect any residual flux of the continuum emission and we assume $C_{\text{cont}} = 0$ (except for three systems towards Q 0528–2508, Q 0405–4418, and Q 0643–5041). To estimate the fraction of the BLR covered by a cloud, we have to correct the covering factor f by the ratio $F_{\text{tot}}/F_{\text{BLR}}$.

$$f_{\text{cov}} = 1 - \frac{F_{\text{add}}}{F_{\text{BLR}}} = 1 - \text{LFR} \frac{(1 + X)}{X} \quad (5)$$

The factor X is the ratio of the BLR flux to the continuum flux of the quasar. The procedure is illustrated in Fig. 1 using the quasar composite spectrum of Vanden Berk et al. (2001). In the top panel, we show the reconstructed continuum; in the bottom panel, we show the normalized composite spectrum and the X function.

¹The accretion disc must be covered completely by the H₂ cloud; otherwise, we would not detect H₂ absorption lines on top of the quasar continuum.

In several spectra, the C I absorption lines associated with the H₂-bearing system are located on top of quasar emission lines. Therefore, we can use the residual flux measured in the C I lines to estimate the BLR covering factor. If partial coverage is a geometrical effect, the BLR covering factors f_{cov} measured on top of different emission lines should be similar. This is what we observe in the case of Q 1232+0815 (see Fig. A12). The LFRs measured in the core of H₂ and C I lines (Balashev et al. 2011) are in good agreement with our estimate of the fraction of the BLR flux that passes by the cloud, which is given by $X(\lambda)/(1 + X(\lambda)) \times (1 - f_{\text{cov}})$. Therefore, either of the C I or H₂ lines may be used to estimate the covering factor of the BLR.

Partial coverage of the quasar continuum source was found only in three H₂ systems in the spectra of quasars Q 0528–2508, Q 0405–4418, and Q 0643–5041. We assume that this emission is produced by some extended source in the host galaxy (e.g. star-forming regions). Therefore, the definition of f does not change, $1 - F_{\text{add}}/F_{\text{cont}} = 1 - \text{LFR}$ (fraction of the quasar continuum).

3.4 Covering factor distribution

Results of our covering factor determinations are presented in Table 1. In columns #6 and #7, we indicate the name of the emission line on top of which partial coverage is seen and the species (H₂ or C I) that was used for the residual flux estimate. In columns #8 and #9, we give values of LFR and f_{cov} . In case we do not detect any residual flux, we determine an upper limit. The first part of the table presents the analysis of systems in the S¹ sample, where we searched for partial coverage of the BLR. The second part contains the results of a search for partial coverage of the quasar continuum emission sources in spectra not included in the S¹ sample.

In the following, we will analyse only systems in the S¹ sample. The measured covering factors are shown versus the H₂ column density in the left-hand panel of Fig. 2. The red and blue circles correspond to H₂ clouds with or without C I-associated absorption, respectively. We detect partial coverage for 13 out of 35 H₂ clouds, which corresponds to a probability of 36 ± 8 per cent. For systems where we did not detect partial coverage, we set lower limits that are typically of the order of $f_{\text{cov}} > 0.8$.

We will explore a geometric scenario to describe the effect of partial coverage, although other scenarios are also possible. In the following sections, we compare the sizes of H₂ clouds and quasar BLRs.

3.5 Physical size of H₂ absorbers

The size of an H₂ cloud can be estimated as the ratio of the total hydrogen column density to the number density:

$$l_{\text{cloud}} = \frac{N_{\text{H1}} + 2N_{\text{H2}}}{n(\text{H}) + 2n(\text{H}_2)} = \frac{2N_{\text{H2}}}{n} \times f_{\text{corr}} \quad (6)$$

$n = n(\text{H}) + 2n(\text{H}_2)$ is the total volume gas density, N_{H1} is the column density of the neutral hydrogen associated with the H₂ cloud. We introduce the correction factor

$$f_{\text{corr}} = \frac{N_{\text{H1}} + 2N_{\text{H2}}}{2N_{\text{H2}}} = 1 + \frac{N_{\text{H1}}}{2N_{\text{H2}}} \quad (7)$$

which is the inverse of the hydrogen molecular fraction in the H₂ cloud $f_{\text{H}_2} = 2N_{\text{H}_2}/(N_{\text{H1}} + 2N_{\text{H}_2})$.

The number density can be estimated from the analysis of the C I fine structure excitation (Silva & Viegas 2002), while the correction

factor may be determined only theoretically. The column density of H I gas associated with the H₂ cloud cannot be measured directly from spectroscopic analysis because the different H I components are blended in the damped Lyman- α (DLA) trough.

3.5.1 Number density

In order to constrain the number density, we use the relative populations of the C I fine structure levels (see Silva & Viegas 2002). C I absorption lines are detected in 24 out of 35 H₂ clouds in our sample. Our estimates of the number density are presented in column 10 of Table 1.

We use the same calculation and code as in (Klimenko et al. 2016; Balashev et al. 2017, 2019). Let us consider briefly some assumptions of our model. C I fine structure levels are populated by the cosmic microwave background (CMB) radiation, UV pumping, and collisions. The CMB temperature at redshift z is fixed to $2.725 \times (1 + z)$ K. Collisions occur with species H, H₂, and He. We assume the abundance of He is 0.085, the helium fraction in the Solar system, see Asplund et al. (2009), and the molecular fraction is 0.2, which corresponds to the local molecular fraction in H₂ clouds, calculated using equation (15) at the mean column density $\log N_{\text{H}_2} = 18$ of the systems in the S¹ sample. The exact molecular fraction is actually unknown and is not constant through the cloud. However, the number density estimated using the C I fine-structure excitation is almost insensitive to the choice of the f_{H_2} value because collisions with H₂ molecules are negligible. The variations are smaller than 0.1 dex over the range $0 \leq f_{\text{H}_2} < 0.5$ and $1 < \log n < 4$.

The excitation temperature of H₂ measured from the populations of the $J = 0$ and $J = 1$ rotational levels is used as a proxy for kinetic temperature in the cold interstellar medium (ISM) (Roy, Chengalur & Srikanth 2006). The UV field is taken from Draine (1978) with unit intensity, $I_{\text{UV}} = 1$. Due to the low measured C I column densities, we neglect self-shielding in the C I lines. The number density measured in C I-bearing H₂ systems is shown in the of Fig. 3. Red circles represent systems in the S¹ sample; green circles represent other known C I-bearing H₂ systems in high redshift DLAs [J 0000+0048 (Noterdaeme et al. 2017), J0551–3638, two components in B 1331–0170 (Carswell et al. 2011), J0816+1446, J 1513+0352 (Ranjan et al. 2018), J2140–0321 (Noterdaeme et al. 2015), B2318–1107 (Noterdaeme et al. 2007a)]. We find a correlation between n and N_{H_2} with dispersion ~ 0.3 – 0.4 dex over the range $15 < \log N_{\text{H}_2} < 21$, approximately following the relation

$$\log n \simeq 0.43 + 0.08 \times \log N_{\text{H}_2} \quad (8)$$

For H₂ systems in the S¹ sample where C I has not been detected, we estimate the number density using the above relation (equation 8).

3.5.2 Correction factor

The correction factor may be determined by using a detailed microphysics model of the H I \rightarrow H₂ conversion in a diffuse molecular cloud developed by Sternberg et al. (2014) and Bialy & Sternberg (2016).

To describe the H I \rightarrow H₂ conversion, we follow Bialy & Sternberg (2016) and approximate a cloud as a uniform optically thick slab illuminated by a beamed radiation flux coming from both sides.

In steady-state equilibrium, we can equate the H₂ formation and destruction rates

$$R_{\text{nn}}(\text{H}) = \frac{1}{2} D_0 f_{\text{sh}}(N_{\text{H}_2}) e^{-\sigma_g N} n(\text{H}_2) \quad (9)$$

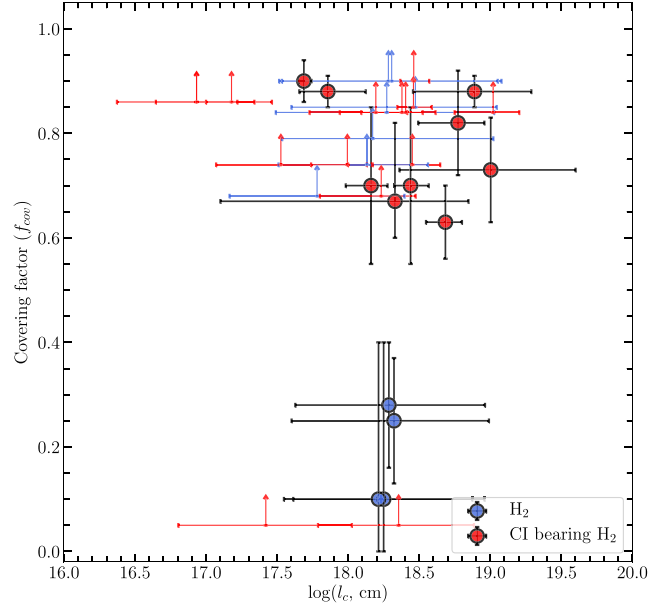
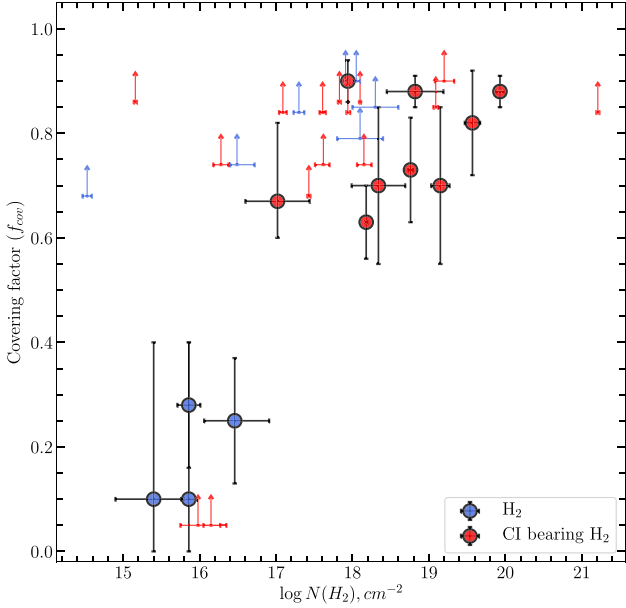


Figure 2. We show covering factors of BLR regions by high redshift H_2 absorption systems as a function of the total H_2 column density (left-hand panel) and the physical size of H_2 clouds (right-hand panel) for systems in the S^1 sample. The circles represent the H_2 systems, in which we found partial coverage and the arrows show the lower limits on the covering factors in systems in which we did not detect partial coverage. Red and blue colours correspond to H_2 systems with and without associated CI absorption.

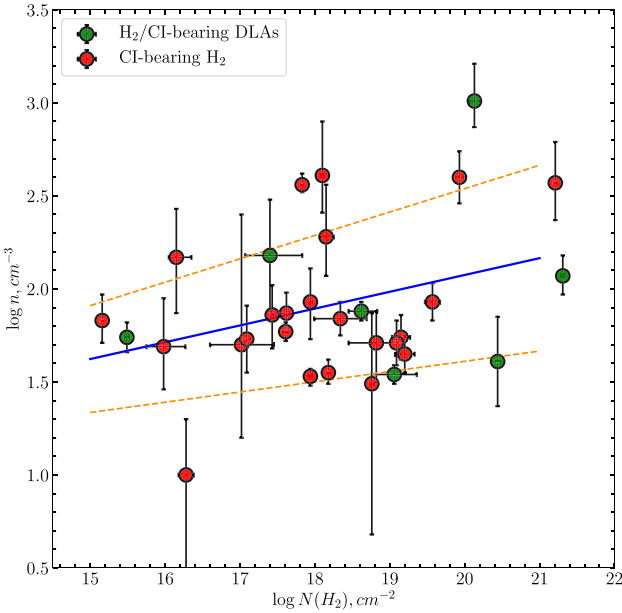


Figure 3. The dependence of the total hydrogen density on the H_2 column density. Red and green circles correspond to the known H_2/CI -bearing DLAs at high redshift in the S^0 sample and in other known DLAs (see text). The blue and orange lines represent the mean hydrogen density and its variance as a function of $N(\text{H}_2)$, measured for this sample.

R is the H_2 formation rate coefficient, D_0 is the free-space photo-dissociation rate, $f_{\text{sh}}(N_{\text{H}_2})$ is the self-shielding factor of H_2 (Draine & Bertoldi 1996), $\sigma_g N$ is the dust opacity in the Lyman–Werner band, where $N = N_{\text{H}_1} + 2N_{\text{H}_2}$, and $\sigma_g = 1.9 \times 10^{-21} \text{cm}^2$ is the effective absorption cross-section by dust per hydrogen nucleus (Draine 2003; Sternberg et al. 2014). A characteristic value for R is

$3 \times 10^{-17} \text{cm}^3 \text{s}^{-1}$ (Jura 1975; Le Petit et al. 2006; Le Bourlot et al. 2012). Introducing the term α (Bialy & Sternberg 2016)

$$\alpha = \frac{D_0}{Rn} = 5.8 \times 10^4 I_{\text{UV}} \left(\frac{10^{-17} \text{cm}^3 \text{s}^{-1}}{R} \right) \left(\frac{100 \text{cm}^{-2}}{n} \right) \quad (10)$$

where I_{UV} is the radiation field relative to the Draine field (Draine 1978); we may rewrite equation (9) as:

$$\frac{n_1}{n_2} = \frac{1}{2} \alpha f_{\text{sh}}(N_2) e^{-\sigma_g(N_1+2N_2)} \quad (11)$$

In this equation, n_1 and n_2 are the local atomic and molecular hydrogen volume densities and N_1 and N_2 are the column densities of atomic and molecular hydrogen on the line of sight. Assuming $dN_1 = \frac{n_1}{n_2} dN_2$, we separate N_1 and N_2 . It is similar to equation (13) in Bialy & Sternberg (2016).

$$dN_1 e^{\sigma_g N_1} = \frac{1}{2} \alpha f_{\text{sh}}(N_2) e^{-2\sigma_g N_2} dN_2 \quad (12)$$

Integration gives

$$N_1 = \frac{1}{\sigma_g} \ln \left(1 + \sigma_g \int_0^{N_2} \frac{1}{2} \alpha f_{\text{sh}}(N_2) e^{-2\sigma_g N_2} dN_2 \right) \quad (13)$$

the column density of HI as a function of $N(\text{H}_2)$. Since we consider the cloud as a slab irradiated from both sides, we integrate from the edge to half of the cloud and then double the result. Therefore, we have

$$N_1 = \frac{2}{\sigma_g} \ln \left(1 + \sigma_g \int_0^{N_2/2} \frac{1}{2} \alpha f_{\text{sh}}(N_2) e^{-2\sigma_g N_2} dN_2 \right) \quad (14)$$

This is the column density of H I envelope on both sides of the H₂ layer. Then, the correction factor is determined as

$$f_{\text{corr}} = 1 + \frac{2}{\sigma_g N_2} \ln \left(1 + I_{\text{UV}} \left(\frac{100 \text{ cm}^{-2}}{n} \right) \left(\frac{10^{-17} \text{ cm}^3 \text{ s}^{-1}}{R} \right) \right) \times \sigma_g \int_0^{N_2/2} 2.9 \times 10^{-4} f_{\text{sh}}(N_2) e^{-2\sigma_g N_2} dN_2 \quad (15)$$

The H₂ column density and number density n can be estimated, but we have no robust constraint on the UV intensity. However, we can set an upper limit on f_{corr} , assuming that all the H I gas in the DLA is associated with the H₂ cloud,

$$f_{\text{corr}} < f_{\text{corr}}(N_{\text{HI}}^{\text{DLA}}) = 1 + N_{\text{HI}}(\text{DLA})/2N_{\text{H}_2} \quad (16)$$

The real molecular cloud has a complex geometry, and the relevance of using a slab model should be discussed here. This question has already been considered by Sternberg et al. (2014) (see Sections 4.1 and 4.2). The authors compared models using a plane-parallel slab and a uniform-density sphere and found that the formation of H₂ is similar in both models (e.g. see fig. 11 in their paper). We use their calculation to estimate a systematic error on the correction factor, which will depend on the choice of the model. Using their definition, the parameter $y = \tau_z/\tau_1$ is the normalized H I dust optical depth. It can be considered as the ratio of the total to the H I column densities $y \sim (N_1 + 2N_2)/N_1$, which is just derived from the spectral analysis. Using equations (97) and (100) in Sternberg et al. (2014), we can calculate the difference between the $f_{\text{corr}} = y/(y - 1)$ parameters calculated for the slab and spherical models as a function of the hydrogen mass fraction (f_{H_2} in their definition). We find that this difference is about -0.5 dex in the logarithmic scale for $f_{\text{H}_2} < 0.5$, i.e. a spherical cloud illuminated by an isotropic UV field is usually three times more compact than a slab exposed to a beamed UV radiation field. We can also estimate the systematic error on f_{corr} corresponding to the choice in the radiation geometry. Switching from beamed to isotropic radiation corresponds to the same difference about -0.5 dex. Therefore, we can estimate the typical systematic error corresponding to the choice of a particular geometry for the cloud and radiation to be -0.5 dex.

3.5.3 Estimate of the physical size of the absorbers

To determine the size of each H₂ system in the S^0 sample, we realize a simulation of 40 000 clouds randomly distributed in parameter space ‘ $\log n - \log I_{\text{UV}}$ ’. The gas density n is normally distributed with mean and variance as we determined using the C I fine structure excitation or based on the relation in equation (8) (for the case where C I has not been detected). The intensity of the UV radiation I_{UV} is uniformly distributed in the range $\log I_{\text{UV}} = [0, 1]$ in units of Draine field.²

Let us name the sample of simulated clouds as the S^{sim} sample. For each cloud in the S^{sim} sample, we calculate the f_{corr} factor and the physical size [using equations (15) and (6)]. Then we exclude from the S^{sim} sample clouds with $f_{\text{corr}} > f_{\text{corr}}(N_{\text{HI}}^{\text{DLA}})$. We

finally estimate the values and statistical errors for f_{corr} and the physical size in the new S^{sim} sample using the maximum likelihood method.

An example of the simulation constructed for the H₂ system in DLA towards J 1237+0647 is shown in top panels of Fig. 4. The left-hand panel of the figure shows the distribution of clouds in the ‘ $\log n - \log I_{\text{UV}}$ ’ plane and the right-hand panel of the figure gives the histogram of the physical sizes calculated for the simulated clouds.

In the middle and bottom panels of Fig. 4, we show our estimates of the correction factor and physical size of clouds in the S^0 sample, respectively. We compare our estimates of f_{corr} (circles) and upper limits (arrows) from observations with the values calculated using equation (15) for three values of $I_{\text{UV}} \times (100 \text{ cm}^{-3}/n) = 1, 10, 100$. The UV intensity $1 < I_{\text{UV}} < 10$ units of Draine field and hydrogen density $n \sim 100 \text{ cm}^{-3}$ satisfy most of the observed points. The correction factor is high (about $10^2 - 10^4$) at low H₂ column densities ($\log N_2 < 18$). This is therefore an important parameter to be taken into account when estimating the size of such clouds.

We show our estimates of the H₂ cloud physical size in the bottom panel. Colours for observed points are the same as in the middle panel. The curves correspond to equation (8) and three values of the UV intensity (1, 10, 100) $\times (n/100 \text{ cm}^{-3})$ times the Draine field. The typical size is pretty constant with an average value of $\log l_c/\text{cm} = 18.2 \pm 0.4$ at column densities $\log N_2 < 18$ and increases slightly at higher H₂ column densities.

3.6 A model of partial coverage

In this section, we present an analytic approach to derive the probability of partial coverage. This idea was previously considered in a recent analysis of partial coverage in a single H₂/C I system towards J 2225+0527 (Krogager et al. 2016).

As before, we assume that (i) the H₂ cloud and BLR region are spherical in shape with radius $R = l_c/2$ and a , respectively, and (ii) the accretion disc located at the centre of the BLR is covered completely. The position of the BLR along the radial coordinate of the cloud (the impact parameter) is defined by the parameter x and varies in the range of $x = 0$ (the centres of the BLR and the cloud coincide) to $x = R$ when the external limit of the cloud and the centre of the BLR are just in contact. We consider that the position of the cloud is fixed, while the BLR is moving. Due to the spherical symmetry, the distribution of the BLR position over the radial coordinate is

$$p(x) = 2x/R^2. \quad (17)$$

The covering factor f_{cov} is a self-similar function of two parameters: $\eta = x/a$ and $\zeta = R/a$. The covering factor depends mainly on $\zeta = R/a$ (see illustration in the left-hand panel of Fig. 5). (i) If the radius of a cloud is less than the half-radius of the BLR ($\zeta < 1/2$), the covering factor is always $f_{\text{cov}} = R^2/a^2$ [x is in the range (0, R)]. (ii) If $1/2 < \zeta \leq 1$, then the covering factor is constant for x in the range (0, $a - R$) and then decreases to value $1/\pi \times \arccos(a/2R)$ at $x = R$. (iii) If $\zeta > 1$, then the covering factor is equal to 1 at $x < R - a$ (the BLR is completely covered by the cloud) and decreases to $1/\pi \times \arccos(a/2R) \simeq 0.43$ for higher values of x . An example of the function $f_{\text{cov}}(x)$ for $\zeta = 1.6$ is shown as the blue curve in the left-hand panel of Fig. 5.

²In our Galaxy, the interstellar UV field was theoretically estimated by several authors: Habing (1968), Mathis, Rumpl & Nordsieck (1977), and Draine (1978). However, higher values of the UV intensity at high redshift, $z \sim 2$, have sometimes been confirmed by observations of individual DLA systems (see Wolfe, Prochaska & Gawiser 2003; Noterdaeme et al. 2017, 2015; Klimenko et al. 2016; Balashev et al. 2017).

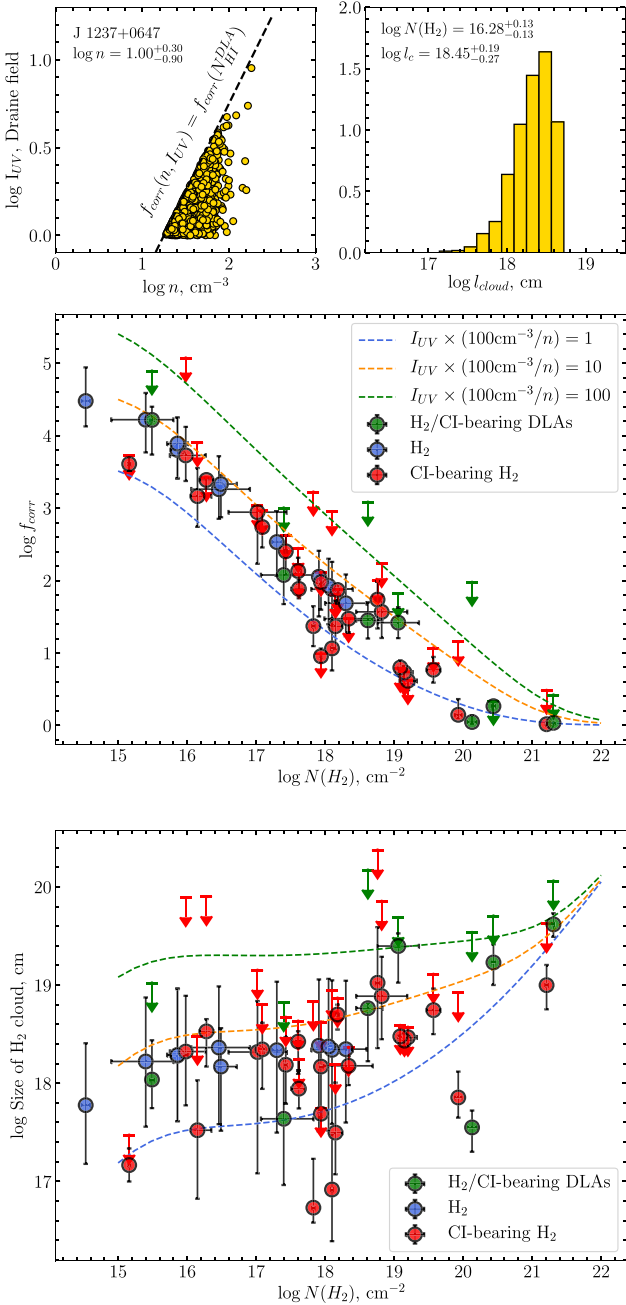


Figure 4. Top: left-hand panel: an example of the simulation of physical conditions in the H_2 systems towards the quasar J 1237+0647. The dashed line corresponds to the upper limit on the value of the correction factor. Right-hand panel: the distribution of the physical size of clouds in that simulation. The best value for the physical size of the cloud is $\log l_c = 18.45^{+0.19}_{-0.27}$. Middle panel: the correction factor f_{corr} as a function of the H_2 column density. The lines represent the analytical function calculated from equation (15) for three values of the UV field, $I_{\text{UV}}(100\text{cm}^{-3}/n) = 1, 10, 100$. The red and blue circles correspond to H_2 systems in the S^1 sample with and without associated C I-detected absorption; the green circles represent other known DLAs at high redshift. Bottom panel: our estimates of the physical size of the clouds in the S^1 sample and other known high redshift DLAs are shown as a function of the H_2 column density. The green, orange, and blue curves correspond to analytical functions calculated using equation (6) for three values of the UV field, $I_{\text{UV}} \times (100\text{cm}^{-3}/n) = 1, 10, 100$.

For fixed ζ , the probability density of $f_{\text{cov}}(\eta, \zeta)$ is given by

$$p(f) = p(x) \frac{dx}{d\eta} \frac{d\eta}{df} = \frac{2a^2 \eta(f) d\eta(f)}{R^2 df} [\theta(f - f(\eta = R/a)) - \theta(f(\eta = 0) - f)] + \delta[f - f(\eta = 0)] \frac{(R-a)^2}{R^2} \quad (18)$$

where $\eta(f)$ is the inverse function $f_{\text{cov}}^{-1}(f(\eta, \zeta))$ and $f(\eta = 0)$ and $f(\eta = R/a)$ are the maximum and minimum values of the covering factor. The inverse function has a singularity at $f(\eta = 0)$, since various positions of the BLR in the range $0 < x < |R - a|$ give the same value of the covering factor; therefore, there is a delta function with a factor of $\int_0^{|R-a|} p(x) dx$.

An example of $p(f)$, calculated at $\zeta = 1.6$, is shown in the middle panel of Fig. 5. In the right-hand panel of Fig. 5, we show the histogram of the probability density of the covering factor f_{cov} as a function of the cloud radius R or ζ . The probability is normalized to the maximum value $\max p(f_{\text{cov}}, \zeta)$ calculated at each ζ . We note that even for large H_2 clouds ($R/a \sim 10-100$), the probability to have the covering factor < 1 is not zero and may be estimated as $\sim 2\pi R a / \pi R^2 \sim 2a/R$.

3.7 Estimate of the BLR size

It would be adventurous to estimate the size of the BLR from the above estimated size of the cloud in individual systems. However, we can estimate a characteristic physical size of the BLRs based on an analysis of the probability of partial coverage in the whole sample.

We want to compare the observed distribution of partial coverage in the S^1 sample with the modelled distribution, which is calculated for a simulated sample of H_2 systems with the same physical size distribution as the S^1 sample but with various physical size of the BLR region. Therefore, we assume:

- (i) The simulated clouds have the same distribution of physical sizes as real clouds in the S^1 sample. The histograms are shown in the left-hand panel of Fig. 6.
- (ii) To describe partial covering effects and calculate the covering factors, we use our model described in Section 3.6.
- (iii) The parameter a in this model is the characteristic BLR size that we want to constrain. We thus let the parameter a vary in the range $(0.01-10) \times R_0$, where R_0 is a half of the average size of H_2 systems in the S^1 sample ($\log R_0/1\text{cm} = 17.87$).

First, for each value of a_k in this range, we generate a sample of physical sizes $\{R_i\}$ of simulated H_2 clouds. The number of systems (i_{max}) was chosen equal to 300 in order to obtain a smooth distribution of covering factors. Then for each i 'th cloud, we generate random positions of the BLR in the range $0 \leq x \leq R_i$ with density $p(x) = 2x/R_i^2$ and calculate the covering factor f_{ik} . During this operation, the radius of the BLR a_k was fixed. Thus, we constructed a sample of $\{f_{ik}(a_k)\}$, associated with the characteristic BLR size a_k . Secondly, we compare the distribution of the sample $\{f_{ik}(a_k)\}$ and the distribution of $\{f_{\text{cov}}\}$ for the S^1 sample (see Table 1) using the Kolmogorov–Smirnov (KS) criteria.

The result is shown in Fig. 6. In the middle panel, we show the cumulative distribution function for the covering factors of the S^1 sample and for the best-fit simulation (at $\log a/R_0 = -0.76$). The difference is shown by green dashed line. In the right-hand panel, we show the P value (blue line) and KS statistic (orange line). We find that distributions for the S^1 sample and simulation are consistent at the level of 68 per cent for $\log a/R_0 = -0.76^{+0.15}_{-0.25}$. Therefore, we estimate the characteristic BLR radius to be $R_{\text{BLR}} = a = 1.3^{+0.5}_{-0.6} \times 10^{17} \text{cm} = 0.04^{+0.02}_{-0.02} \text{pc}$.

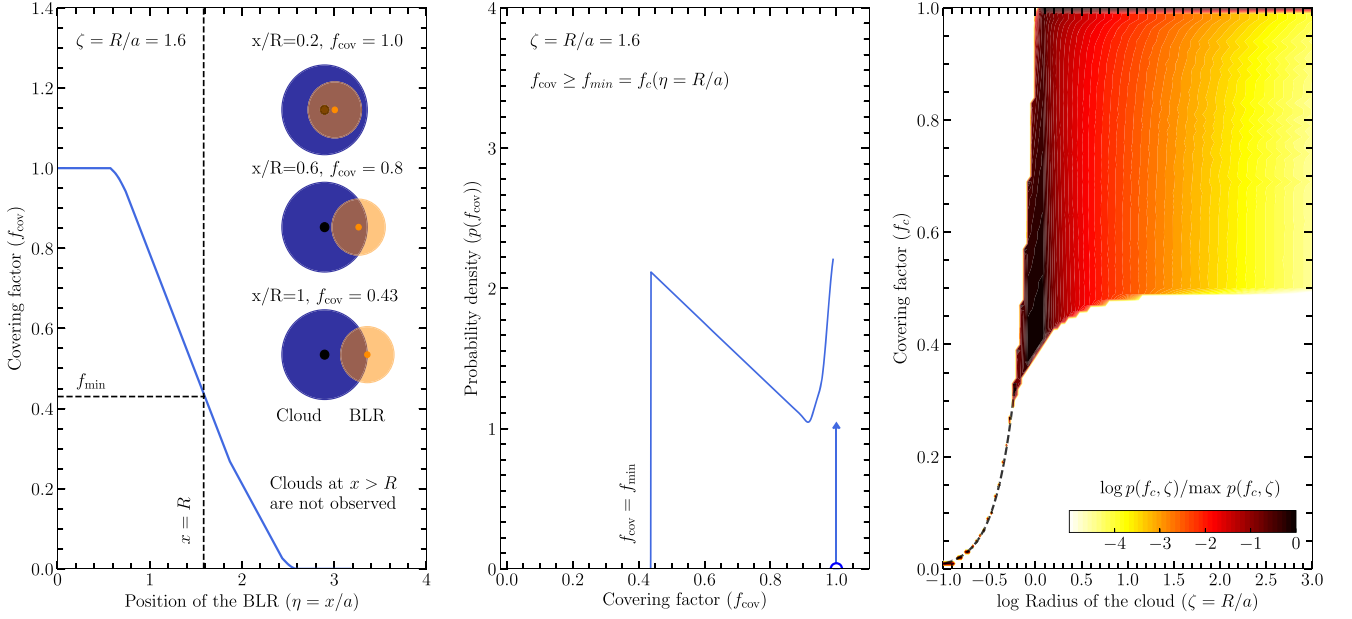


Figure 5. Left-hand panel: an example of the dependence of the covering factor of a BLR (f_{cov}) on the position of the BLR ($\eta = x/a$) along the radial coordinate of the cloud (blue line). The sizes of the BLR and cloud are chosen to be $\zeta = R/a = 1.6$ and $a = 1$. The illustrations show the location of the cloud and BLR at three values of x/R , 0.2, 0.6, and 1. The blue and orange circles represent the H₂ cloud and BLR. The vertical dashed line represents the upper limit on the position of the BLR. Middle panel: the probability density of the covering factor calculated at $\zeta = 1.6$. The function has a singularity at $f_{\text{cov}} = 1$. Right-hand panel: The interpolation of the normalized probability density of f_{cov} as a function of the $\zeta = R/a$ and the value of the covering factor. The value of the probability density relative to its maximum value at fixed ζ is indicated by the colour in log scale.

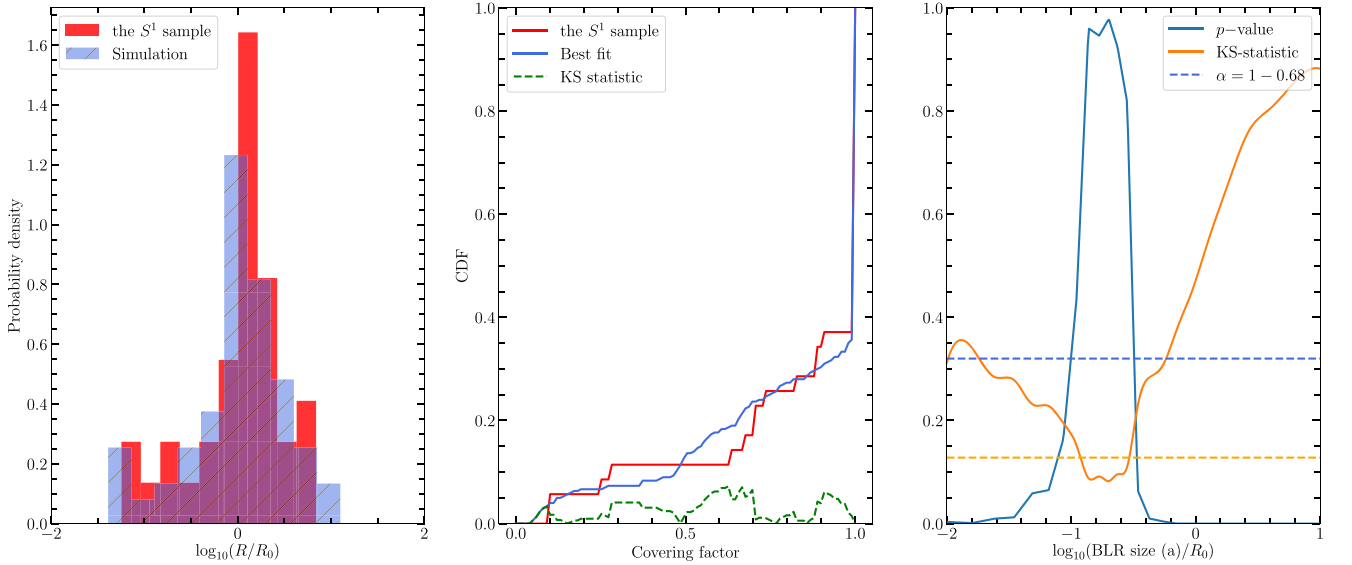


Figure 6. Left-hand panel: red and blue histograms represent the distributions of the size of the H₂ systems in the S^1 sample and the simulation. Middle panel: We show the cumulative distribution of the covering factor calculated for the S^1 sample (red) and the simulation (blue) at $\log a/R_0 = -0.76$ (the best-fitting value). The green line is the difference between the two cumulative functions. Right-hand panel: We present the result of a Kolmogorov–Smirnov test by the p -value (blue line), KS-statistic (orange line) and the P value (blue line). The dashed blue and orange horizontal lines represent the significance level $\alpha = 0.32$ (at 1σ) and the critical value K_{α} , accordingly.

4 CONCLUSION

We have studied the partial coverage of quasar emission by intervening H₂ clouds. We have analysed 18 high-resolution quasar spectra

obtained with the VLT and Keck telescopes and found four new cases of partial coverage in addition to eight already known. The new H₂ systems with partial coverage are towards Q0013–0029, Q0405–4418, Q0812+3208, and J2100–0641. We selected a

sample of H₂ clouds (the S¹ sample), for which we are able to detect partial coverage of the BLR region with a high significance. The sample contains 35 H₂ clouds in 14 quasar spectra. The list of the systems is presented in Table 1. We detect partial coverage of the BLR region in 13 out of 35 H₂ clouds. This corresponds to a probability of 36 ± 8 per cent. For other systems, we set lower limits on the covering factor at the level of about $f_{\text{cov}} \geq 0.8$.

Then we derived the physical size of H₂ clouds in the S¹ sample using an estimate of the hydrogen density based on the analysis of the C I excitation (Silva & Viegas 2002) and a micro-physics model of H₂ formation (Bialy & Sternberg 2016). The average size of H₂ clouds in the S¹ sample is found to be $\log l_0/1 \text{ cm} = 18.2$ and the variance is $\sigma_0 = 0.4$.

We simulated the partial coverage effect for a sample of clouds similar to the S¹ sample and estimated the characteristic size of the BLR that reproduces the observed distribution of covering factors:

$$R_{\text{BLR}} = 1.3_{-0.6}^{+0.5} \times 10^{17} \text{ cm} = 0.04_{-0.02}^{+0.02} \text{ pc} \simeq 50_{-23}^{+19} \text{ light days} \quad (19)$$

This is to be compared with estimates from reverberation mapping studies. The typical luminosity of high-*z* DLA-bearing quasars in the Sloan Digital Sky Survey Data Release 14 (SDSS DR14) catalogue (Pâris et al. 2018), is $\log \lambda L_{\lambda}(1350\text{\AA})/\text{erg s}^{-1} \sim 45.6_{-0.3}^{+0.7}$. The Kaspi et al. (2017) relation between luminosity and BLR radius gives a corresponding estimate of the BLR size from reverberation mapping of ~ 100 light days, which is consistent with the above estimate.

In summary, partial coverage of the BLR by H₂-bearing intervening clouds is a common effect and its analysis gives us a unique opportunity to investigate the size and structure of the BLR of distant quasars. More should be done to derive the physical state in the ISM of high redshift galaxies (e.g. Noterdaeme et al. 2012) in order to better constrain the models and obtain data of higher quality.

ACKNOWLEDGEMENTS

This work is supported by RFBR grant 18-52-15021. The authors thank S. A. Balashev for useful comments and the anonymous referee for helpful comments and suggestions that improved the presentation of this manuscript.

REFERENCES

Albornoz Vásquez D., Rahmani H., Noterdaeme P., Petitjean P., Srianand R., Ledoux C., 2014, *A&A*, 562, A88
 Asplund M., Grevesse N., Sauval A. J., Scott P., 2009, *ARA&A*, 47, 481
 Balashev S. A., Ivanchik A. V., Varshalovich D. A., 2010, *Astron. Lett.*, 36, 761
 Balashev S. A., Petitjean P., Ivanchik A. V., Ledoux C., Srianand R., Noterdaeme P., Varshalovich D. A., 2011, *MNRAS*, 418, 357
 Balashev S. A., Zavarygin E. O., Ivanchik A. V., Telikova K. N., Varshalovich D. A., 2015, *MNRAS*, 458, 2188
 Balashev S. A. et al., 2017, *MNRAS*, 470, 2890
 Balashev S. A. et al., 2019, *MNRAS*, 490, 2668
 Barlow T. A., Hamann F., Sargent W. L. W., 1997, in Arav N., Shlosman I., Weymann R. J., eds, ASP Conf. Ser. Vol. 128., Mass Ejection from Active Galactic Nuclei. Astron. Soc. Pac., San Francisco, p. 13
 Bergeron J., Boissé P., 2017, *A&A*, 604, A37
 Bialy S., Sternberg A., 2016, *ApJ*, 822, 83
 Carswell R. F., Jorgenson R. A., Wolfe A. M., Murphy M. T., 2011, *MNRAS*, 411, 2319
 Dai X., Kochanek C. S., Chartas J., Kozłowski S., Morgan C. W., Garmire G., Agol E., 2010, *ApJ*, 709, 278

Dekker H., D’Odorico S., Kaufer A., Delabre B., Kotłowski H., 2000, in Iye M., Moorwood A. F., eds, Proc. Vol. 4008, Optical and IR Telescope Instrumentation and Detectors. SPIE, Bellingham, p. 534
 Draine B. T., 1978, *ApJS*, 36, 659
 Draine B. T., 2003, *ARA&A*, 41, 241
 Draine B. T., Bertoldi F., 1996, *ApJ*, 468, 269
 Ellison S. L., Ibata R., Pettini M., Lewis G. F., Aracil B., Petitjean P., Srianand R., 2004, *A&A*, 414, 79
 Ellison S. L., Lewis G. F., Pettini M., Sargent W. L. W., Chaffee F. H., Foltz C. B., Rauch M., Irwin M. J., 1999, *PASP*, 111, 946
 Goodman J., Weare J., 2010, *Comm. App. Math. Comp. Sci.*, 5, 65
 Guimarães R., Noterdaeme P., Petitjean P., Ledoux C., Srianand R., López S., Rahmani H., 2012, *AJ*, 143, 147
 Habing H. J., 1968, *Bull. Astron. Inst. Netherlands*, 19, 421
 Ivanchik A. V., Petitjean P., Balashev S. A., Srianand R., Varshalovich D. A., Ledoux C., Noterdaeme P., 2010, *MNRAS*, 404, 1583
 Jorgenson R. A., Wolfe A. M., Prochaska J. X., 2010, *ApJ*, 722, 460
 Jura M., 1975, *ApJ*, 197, 575
 Kaspi S., Brandt W. N., Maoz D., Netzer H., Schneider D. P., Shemmer O., 2017, *Frontiers Astron. Space Sci.*, 4, 31
 Klimenko V. V., Balashev S. A., Ivanchik A. V., Ledoux C., Noterdaeme P., Petitjean P., Srianand R., Varshalovich D. A., 2015, *MNRAS*, 448, 280
 Klimenko V. V., Balashev S. A., Ivanchik A. V., Varshalovich D. A., 2016, *Astron. Lett.*, 42, 137
 Krogager J.-K., Fynbo J. P. U., Noterdaeme P., Zafar T., Møller P., Ledoux C., Krühler T., Stockton A., 2016, *MNRAS*, 455, 2698
 Le Bourlot J., Le Petit F., Pinto C., Roueff E., Roy F., 2012, *A&A*, 541, A76
 Ledoux C., Petitjean P., Srianand R., 2003, *MNRAS*, 346, 209
 Ledoux C., Petitjean P., Srianand R., 2006, *ApJ*, 640, L25
 Ledoux C., Srianand R., Petitjean P., 2002, *A&A*, 392, 781
 Le Petit F., Nehmé C., Le Bourlot J., Roueff E., 2006, *ApJS*, 164, 506
 Mathis J. S., Rumpel W., Nordsieck K. H., 1977, *ApJ*, 217, 425
 Muzahid S., Srianand R., Arav N., Savage B. D., Narayanan A., 2013, *MNRAS*, 431, 2885
 Noterdaeme P., Petitjean P., Ledoux C., López S., Srianand R., Vergani S. D., 2010, *A&A*, 523, A80
 Noterdaeme P., Petitjean P., Srianand R., Ledoux C., Le Petit F., 2007a, *A&A*, 469, 425
 Noterdaeme P., Ledoux C., Petitjean P., Le Petit F., Srianand R., Smette A., 2007b, *A&A*, 474, 393
 Noterdaeme P., Srianand R., Rahmani H., Petitjean P., Pâris I., Ledoux C., Gupta N., López S., 2015, *A&A*, 577, A24
 Noterdaeme P. et al., 2012, *A&A*, 540, A63
 Noterdaeme P. et al., 2017, *A&A*, 597, A82
 Ofengeim D. D., Balashev S. A., Ivanchik A. V., Kaminker A. D., Klimenko V. V., 2015, *Ap&SS*, 359, 26
 Petitjean P., Aracil B., Srianand R., Ibata R., 2000, *A&A*, 359, 457
 Petitjean P., Rauch M., Carswell R. F., 1994, *A&A*, 291, 29
 Petitjean P., Srianand R., Ledoux C., 2002, *MNRAS*, 332, 383
 Pâris I. et al., 2018, *A&A*, 613, A51
 Ranjan A. et al., 2018, *A&A*, 618, A184
 Roy N., Chengalur J. N., Srianand R., 2006, *MNRAS*, 365, L1
 Silva A. I., Viegas S. M., 2002, *MNRAS*, 329, 135
 Srianand R., Noterdaeme P., Ledoux C., Petitjean P., 2008, *A&A*, 482, L39
 Srianand R., Shankaranarayanan S., 1999, *ApJ*, 518, 672
 Sternberg A., Le Petit F., Roueff E., Le Bourlot J., 2014, *ApJ*, 790, 10
 Vanden Berk D. E. et al., 2001, *AJ*, 122, 549
 Vogt S. S. et al., 1994, in Crawford D. L., Craine E. R., eds, Proc. SPIE Conf. Ser. Vol. 2198, Instrumentation in Astronomy VIII. SPIE, Bellingham, p. 362
 Wolfe A. M., Prochaska J. X., Gawiser E., 2003, *ApJ*, 593, 215

APPENDIX A: FIT TO THE H₂ ABSORPTION LINES AND ANALYSIS OF RESIDUAL FLUX

Figs A1–A12 present portions of spectra of Q0013–0029, Q0405–4418, Q0812+3208, and J2100–0641 around the posi-

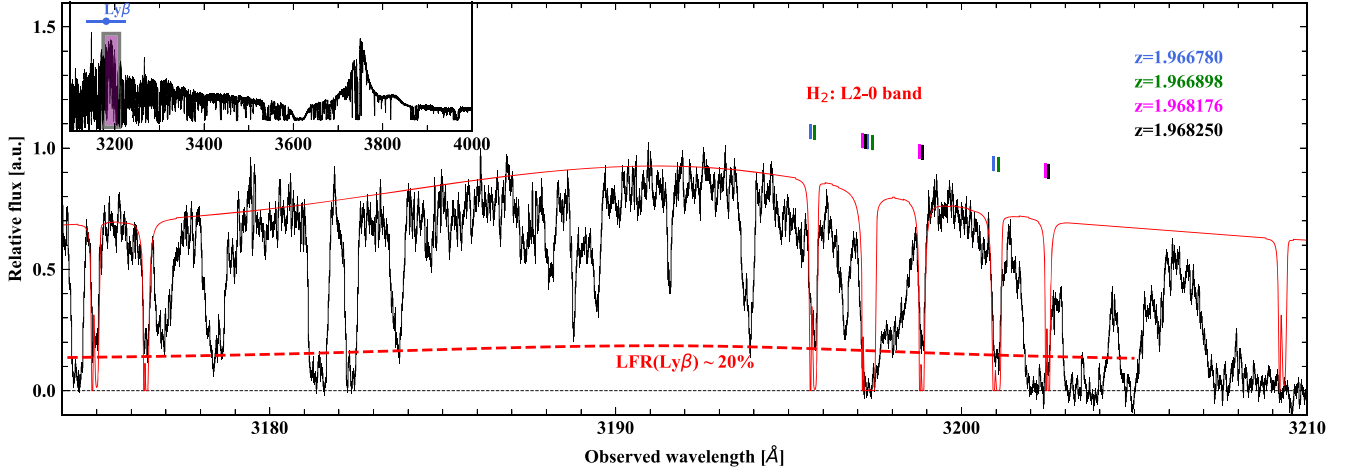


Figure A1. Portion of Q0013–0029 spectrum around the position of Ly β -O IV emission line. Blue, magenta, green, and black sticks represent the positions of H₂ L2-0 from $J=0$ and $J=1$ lines for the three components at $z_{\text{abs}} = 1.966780$, $z_{\text{abs}} = 1.966898$, $z_{\text{abs}} = 1.968176$, and $z_{\text{abs}} = 1.968250$, respectively. The red line represents the best fit without taking into account partial coverage. The fit in the cores of these lines falls under the observed flux. It is due to partial coverage of the Ly β emission region by the H₂ clouds. The best-fitting values for the residual fluxes are about 30, 17, and 28 per cent of the total quasar flux. In Fig. A2, we show the H₂ line profiles for all H₂ lines taking into account the partial coverage for lines falling on the top of the quasar Ly β emission.

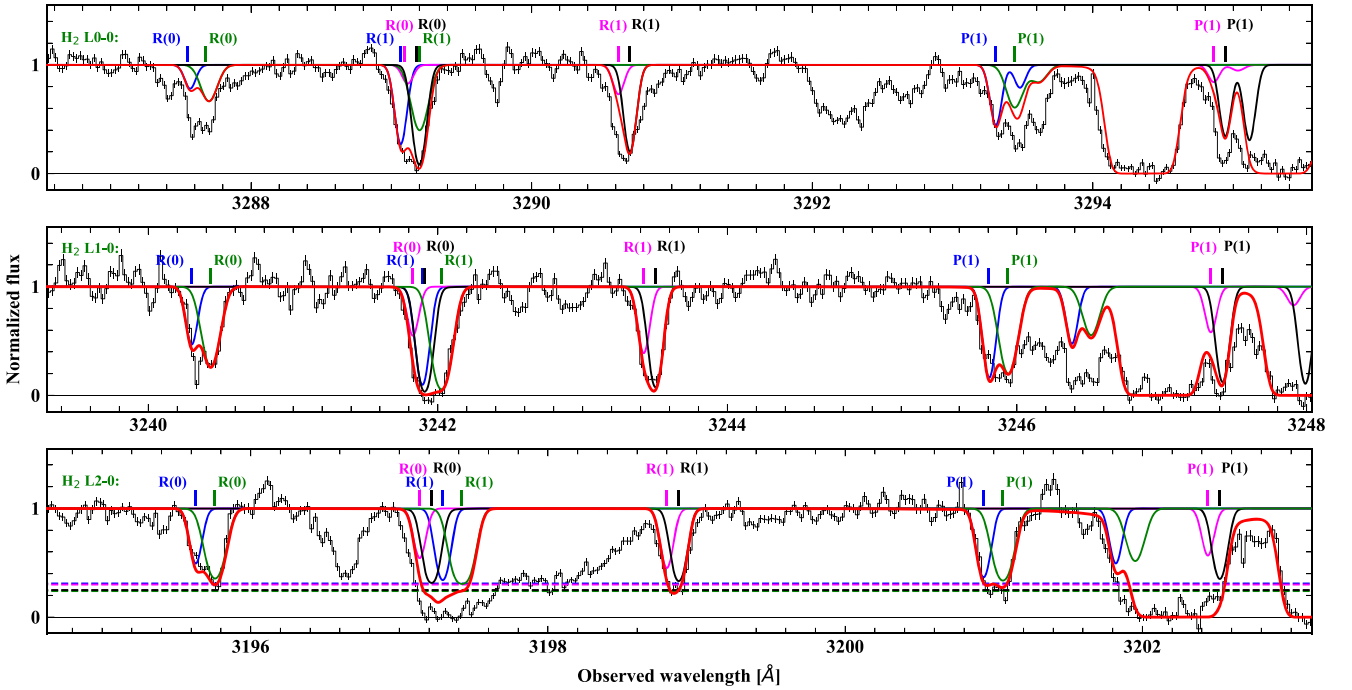


Figure A2. Fit to H₂ $J=0$ and $J=1$ lines at $z_{\text{abs}} = 1.96$ for the first three Lyman bands in the Q0013–0029 spectrum. Positions and profiles of four components at $z_{\text{abs}} = 1.966780$, $z_{\text{abs}} = 1.966898$, $z_{\text{abs}} = 1.968176$, and $z_{\text{abs}} = 1.968250$ are shown by blue, magenta, green, and black colours. The red line represents the full fit. We detect partial coverage of the Ly β BLR. H₂ lines of L2-0 band fall on the top of the Ly β emission line (see Fig. A1). The residual flux in these lines is about 20 per cent of the continuum (see text).

tions of the Ly β emission line, fits to the H₂ absorption lines, and measurements of the residual flux.

The grey dashed line in Figs A3, A5, A10, and A12 represents the normalized X function, defined in Section 3.3 and Fig. 1. The X function was scaled to correspond to observed values of LFR. It is seen that the values of residual flux in H₂ lines (or LFR, blue

points) are well correlated with the flux from the BLR emission (grey line). In addition, we show the known case of BLR partial coverage in the spectrum of Q 1232+0815 (Balashev et al. 2011) in Fig. A12, where we detected the positive correlation of the LFR and X function as well.

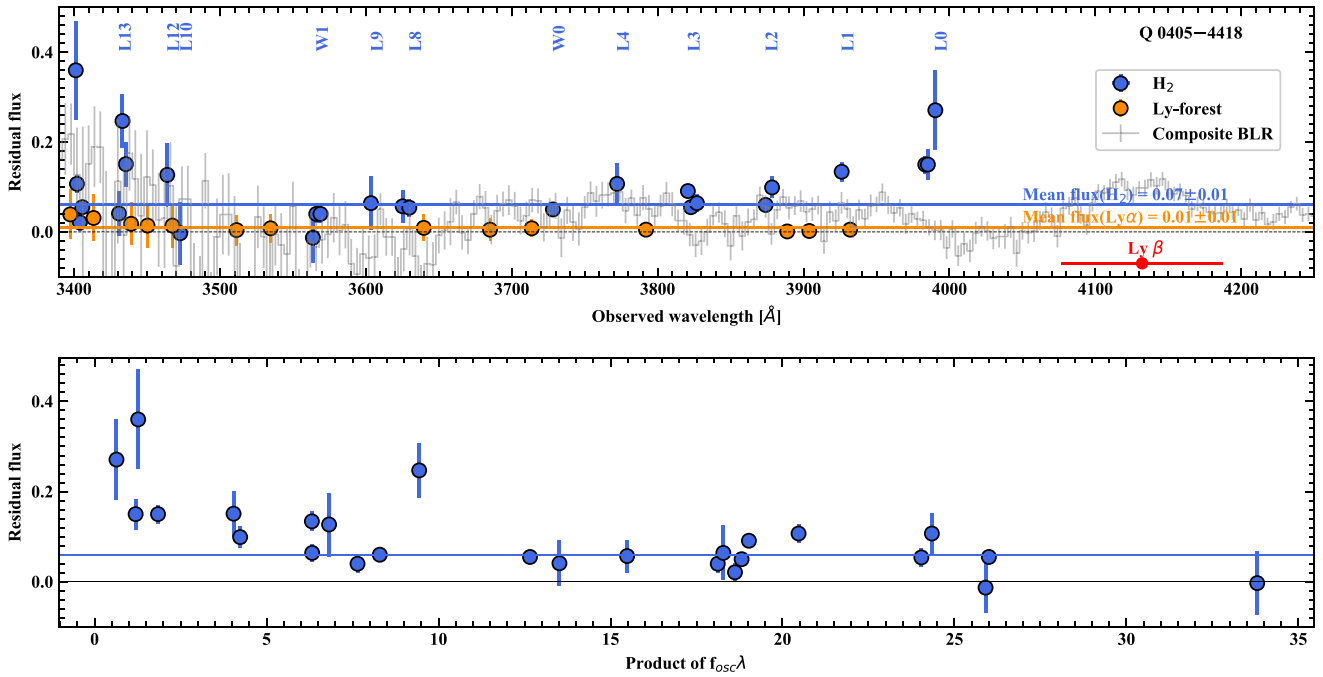


Figure A3. The measurements of the residual flux in the bottom of unblended saturated H₂ absorption lines from $J = 0$ and 1 levels at $z_{abs} = 2.59473$ in the spectrum of Q 0405–4418. Top panel: the residual fluxes in the core of H₂ (blue) and Ly α (orange) lines are shown versus observed wavelength. There is a clear difference between values of the residual flux in H₂ and Ly α . The blue horizontal line represents the best fit to the additional residual flux in H₂ produced by partial coverage of a continuum source. The deviation of blue points from the blue horizontal line at the edges of the wavelength range is due to the dependence of the H₂ oscillator strengths on the wavelength. Bottom panel: The residual fluxes in H₂ lines versus the product of the oscillator strength and wavelength of the transitions. It can be seen that the strongest lines have a residual flux about 7 percent of the continuum. The profiles of H₂ lines are shown in Fig. A4.

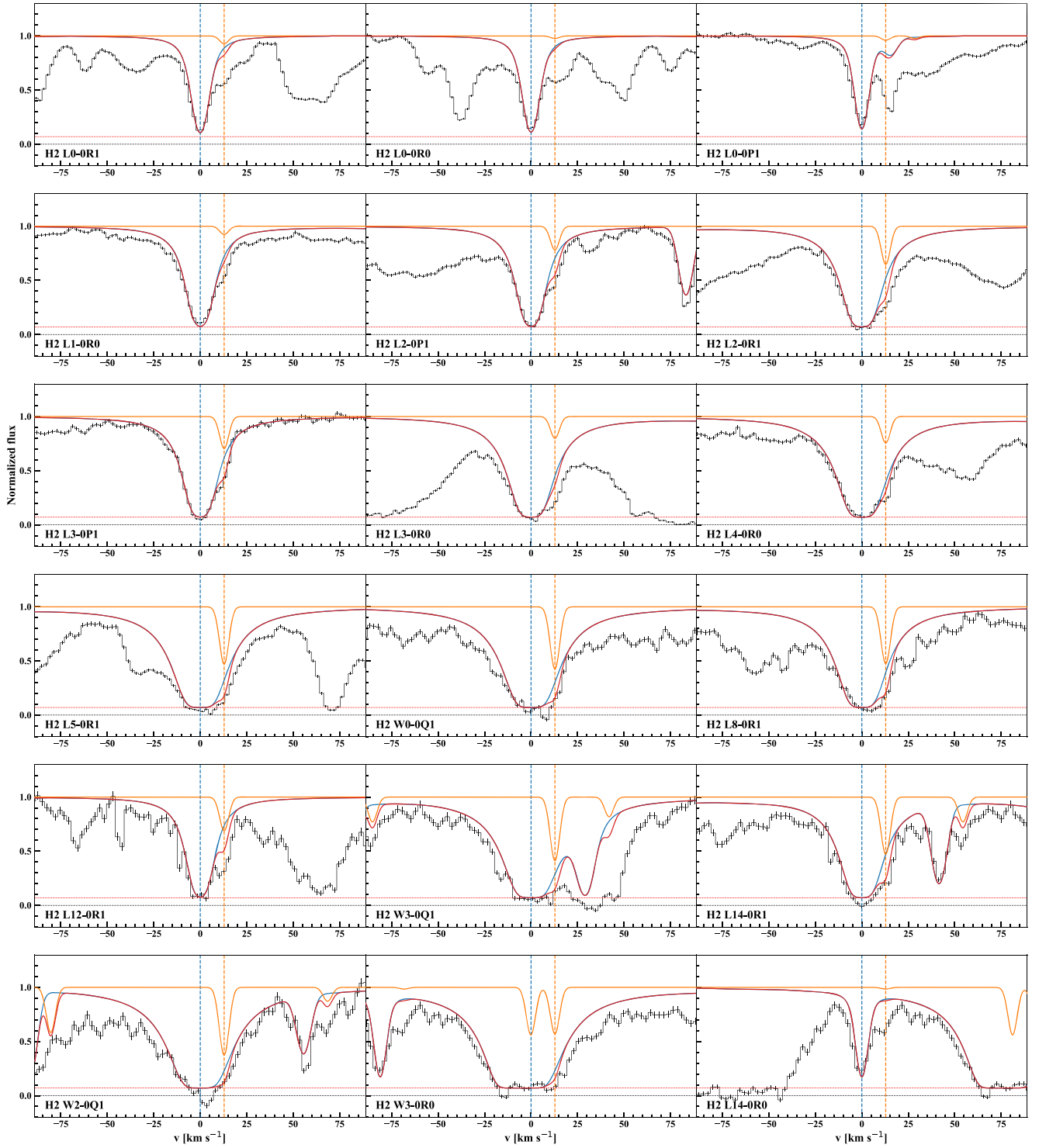


Figure A4. Fit to the H₂ $J = 0$ and $J = 1$ lines in the Q 0405-4418 spectrum (the red line). The profiles of two components are shown by blue (main component) and orange (second component) lines. The value of the residual flux (about 7 per cent) produced by an uncovered continuum source is shown by the red dashed horizontal line.

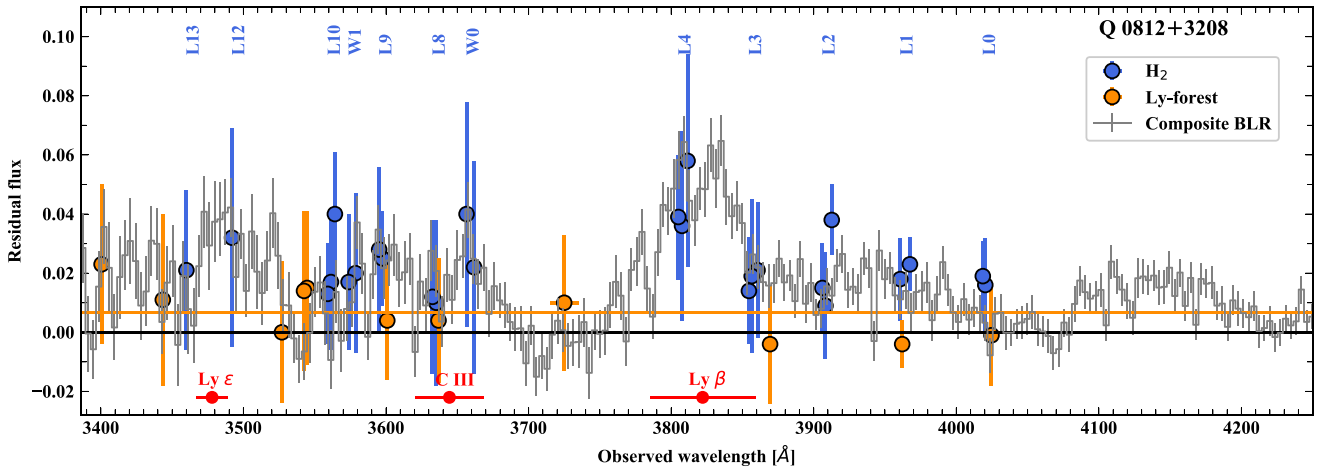


Figure A5. The comparison of the residual fluxes in the cores of H_2 $J=0$ and $J=1$ at $z=2.626$ (blue circles) and $Ly\alpha$ (orange circles) lines in the spectrum of Q 0812+3208 versus the observed wavelength. The position of the $Ly\beta$ emission line is shown by the red circle with error bar. There is a difference between residual fluxes in H_2 lines and $Ly\alpha$ forest lines of about 2 per cent of the continuum. The H_2 lines of L4-0 band falling on to the $Ly\beta$ emission have an increased residual flux of about 4 per cent. The H_2 profiles of L0-0, L1-0, and L4-0 bands are shown in Figs A6–A8.

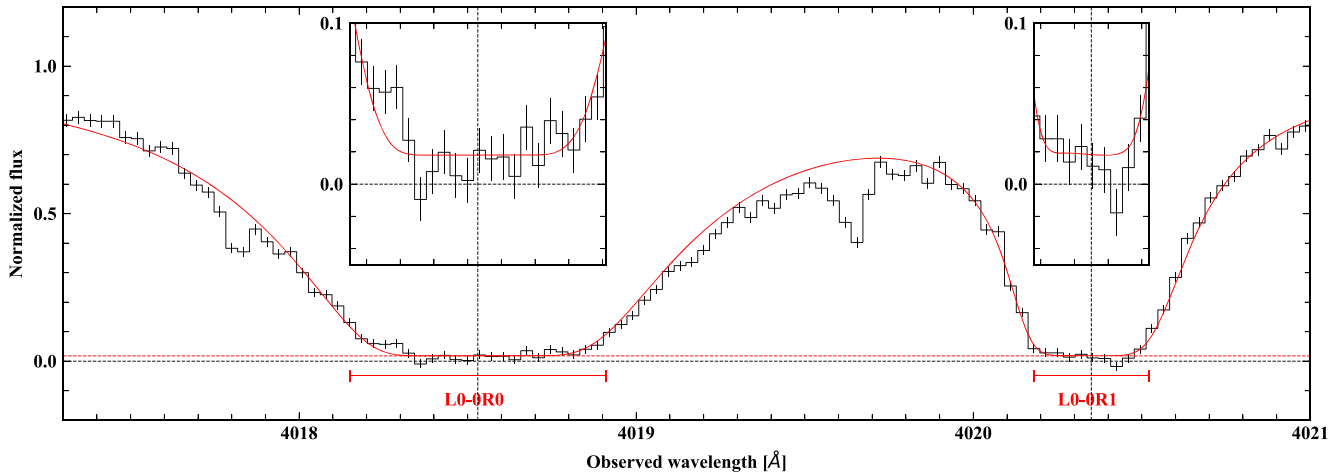


Figure A6. Part of the normalized spectrum of Q 0812+3208 near the position of the L0-0 H_2 band ($z=2.626$). The spectrum and fit to H_2 lines are shown by black and red lines. The red horizontal line represents the value of residual flux in the core of H_2 lines. In the inserted panels, we show the fit at the bottom of the lines in more details. It can be seen that there is a non-zero residual flux in the core of these lines.

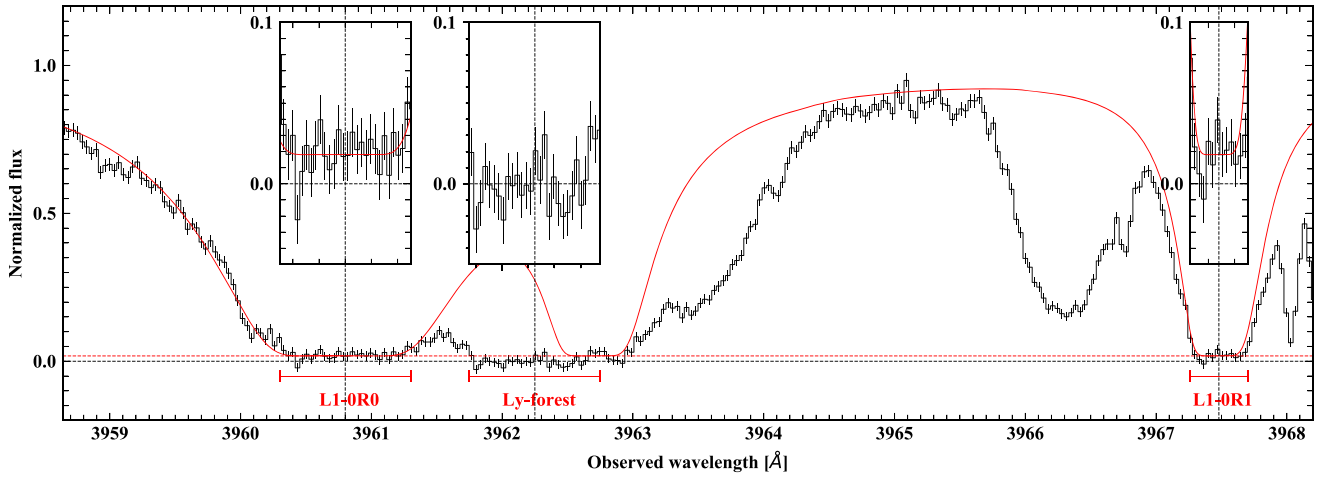


Figure A7. Part of the normalized spectrum of Q0812+3208 near the position of the L1-0 H₂ band ($z = 2.626$). The spectrum and fit to H₂ lines are shown by black and red lines. The red horizontal line represents the value of the residual flux in the core of H₂ lines. In inserted panels, we show the fit at the bottom of the lines in more details. We can see a saturated absorption blend at wavelength 3962.5 Å. The flux in the core of this line goes to the zero level whereas nearby H₂ lines show non-zero residual flux.

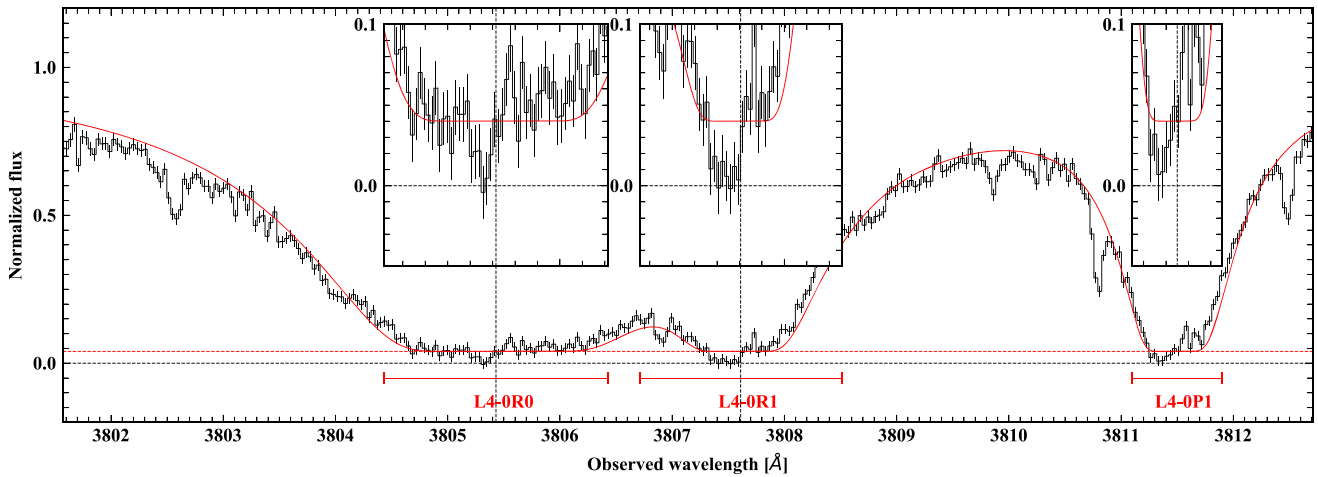


Figure A8. Fit to the H₂ $J = 0$ and $J = 1$ absorption lines in L4-0 band. In the core of the H₂ lines, we detect a residual flux of about 4 percent of the continuum.

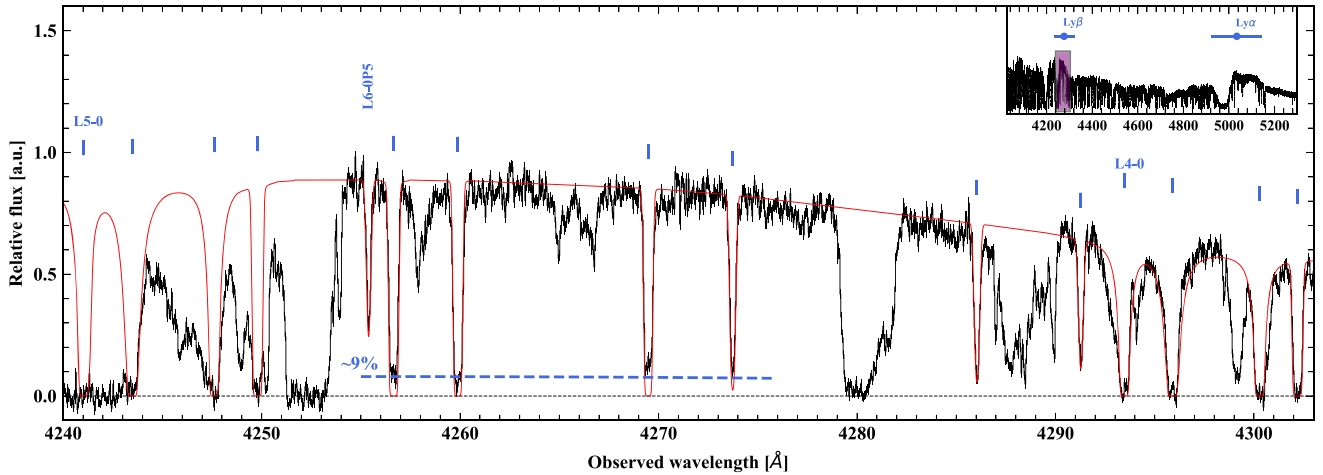


Figure A9. Portion of the J2100–0641 spectrum around the position of the $\text{Ly}\beta$ -O IV emission line. Blue sticks represent the positions of the H_2 L5-0 lines for the component at $z_{\text{abs}} = 3.092$. The red line represents the fit of H_2 lines without taking into account partial coverage. The fit in the core of the H_2 lines falls under the observed flux. The position of an additional flux from an uncovered part of the BLR is shown by the blue dashed line. The profiles of the H_2 lines are shown in Fig. A11.

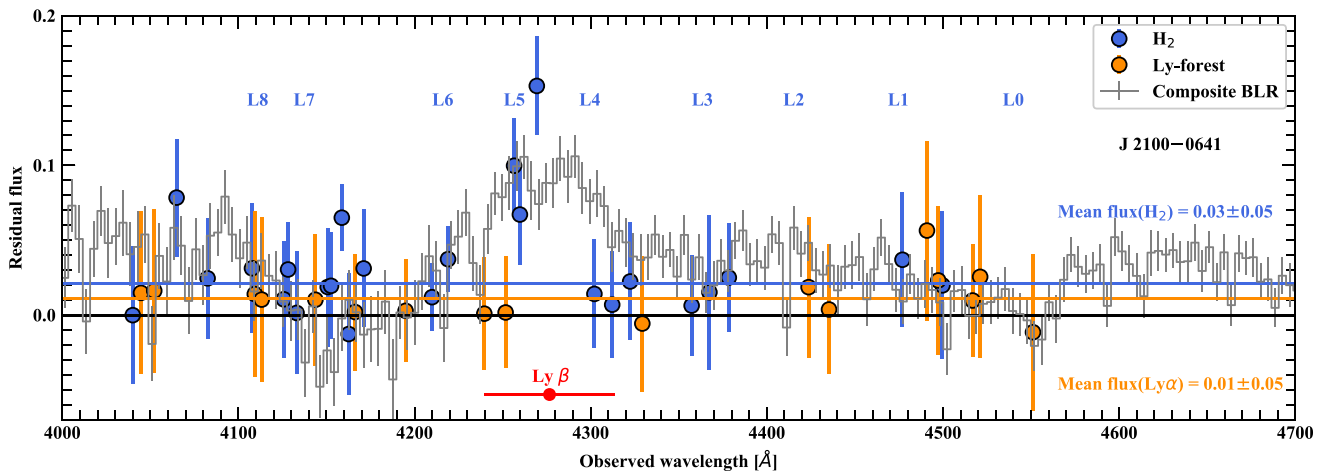


Figure A10. The comparison of the residual fluxes in the core of H_2 $J = 2$ and $J = 3$ at $z = 3.092$ (blue circles) and $\text{Ly}\alpha$ (orange circles) lines in the spectrum of J2100–0641 versus the observed wavelength. The position of the $\text{Ly}\beta$ emission line is shown by the red circle with the error bar. There is a difference between residual fluxes in H_2 lines and $\text{Ly}\alpha$ forest lines of about 1 per cent of the continuum. The H_2 lines of the L5-0 band falling on top of the $\text{Ly}\beta$ emission have an increased residual flux of about 9 per cent.

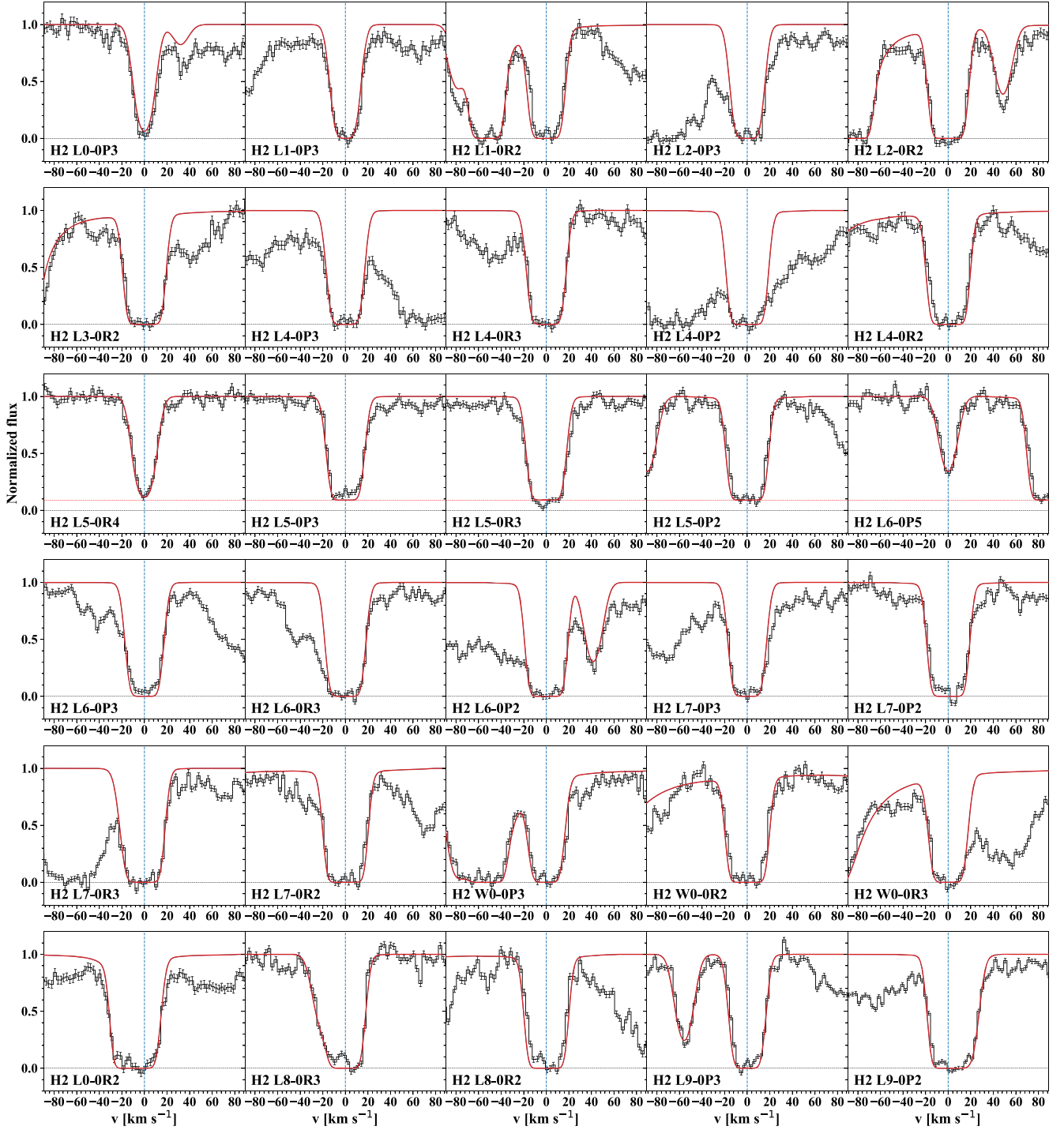


Figure A11. Fit to the H₂ lines at $z_{\text{abs}} = 3.092$ in the J2100–0641 spectrum. In the core of the H₂ lines of L5–0 Lyman band, we detect a residual flux produced by the partial covering of the Ly β BLR, whereas the flux in the core of other H₂ lines goes to the zero level. The value of the residual flux is about 10 per cent of continuum, that is shown by the red horizontal line.

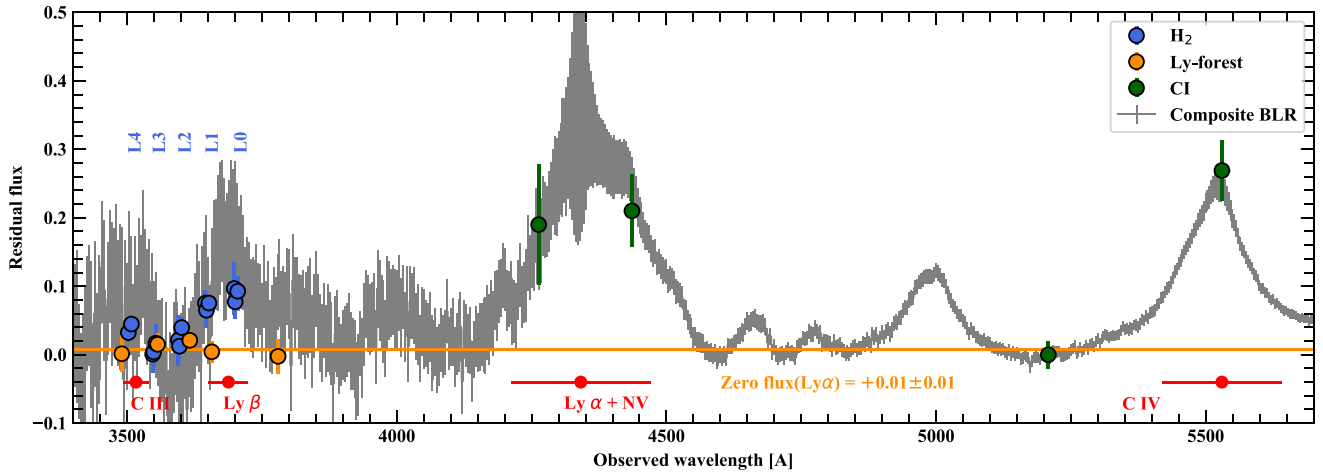


Figure A12. The comparison of the residual flux in the core of H_2 $J = 0$ and $J = 1$ lines at $z = 2.3377$ (blue circles) and the $Ly\alpha$ forest lines (orange circles) in the spectrum of Q 1232+0812 versus the observed wavelength. The position of the $Ly\beta$ and C III emission lines is shown by red circles with error bar. The H_2 lines of L0-0 and L1-0 bands falling on top of the $Ly\beta$ emission have an increased residual flux by about 10 per cent.

This paper has been typeset from a $\text{\TeX}/\text{\LaTeX}$ file prepared by the author.